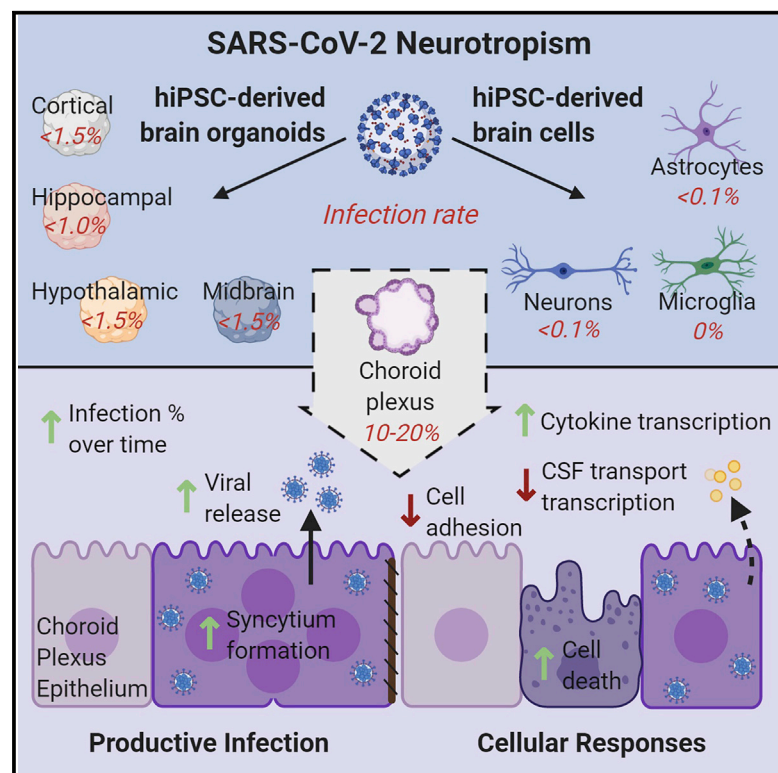# Human Pluripotent Stem Cell-Derived Neural Cells and Brain Organoids Reveal SARS-CoV-2 Neurotropism Predominates in Choroid Plexus Epithelium

Graphical Abstract

Authors

Fadi Jacob, Sarshan R. Pather, Wei-Kai Huang, ..., Hongjun Song, Juan Carlos de la Torre, Guo-li Ming

Correspondence

abang@sbpdiscovery.org (A.G.B.),
shongjun@pennmedicine.upenn.edu (H.S.),
juanct@scripps.edu (J.C.d.l.T.),
gming@pennmedicine.upenn.edu (G.-l.M.)

In Brief

SARS-CoV-2 causes neurological symptoms in a significant portion of patients with COVID-19. Ming and colleagues tested SARS-CoV-2 neurotropism by using monolayer neural cells and brain organoids generated from human pluripotent stem cells and show minimal neuron and astrocyte infection but efficient choroid plexus infection, leading to cell death and functional deficits.

Highlights

- SARS-CoV-2 minimally infects human neurons and astrocytes in 2D and brain organoids

- Model developed for hiPSC-derived choroid plexus organoids (CPOs)

- SARS-CoV-2 productively infects CPOs and increases cell death

- SARS-CoV-2 CPO infection leads to transcriptional upregulation of inflammatory genes

CellPress

Cell Stem Cell

CellPress

Short Article

Human Pluripotent Stem Cell-Derived Neural Cells and Brain Organoids Reveal SARS-CoV-2 Neurotropism Predominates in Choroid Plexus Epithelium

Fadi Jacob,[1,2,3] Sarshan R. Pather,[4] Wei-Kai Huang,[1,5] Feng Zhang,[1] Samuel Zheng Hao Wong,[1,6] Haowen Zhou,[7] Beatrice Cubitt,[8] Wenqiang Fan,[1] Catherine Z. Chen,[9] Miao Xu,[9] Manisha Pradhan,[9] Daniel Y. Zhang,[10] Wei Zheng,[9] Anne G. Bang,[7,*] Hongjun Song,[1,11,12,13,*] Juan Carlos de la Torre,[8,*] and Guo-li Ming[1,11,12,14,15,*]

[1]Department of Neuroscience and Mahoney Institute for Neurosciences, Perelman School of Medicine, University of Pennsylvania, Philadelphia, PA 19104, USA
[2]The Solomon H. Snyder Department of Neuroscience, Johns Hopkins University School of Medicine, Baltimore, MD 21205, USA
[3]Medical Scientist Training Program, Johns Hopkins University School of Medicine, Baltimore, MD 21205, USA
[4]Cell and Molecular Biology Graduate Group, Perelman School of Medicine, University of Pennsylvania, Philadelphia, PA 19104, USA
[5]Graduate Program in Pathobiology, Johns Hopkins University School of Medicine, Baltimore, MD 21205, USA
[6]Graduate Program in Cellular and Molecular Medicine, Johns Hopkins University School of Medicine, Baltimore, MD 21205, USA
[7]Conrad Prebys Center for Chemical Genomics, Sanford Burnham Prebys Medical Discovery Institute, 10901 North Torrey Pines Road, La Jolla, CA 92037, USA
[8]Department of Immunology and Microbiology, The Scripps Research Institute, La Jolla, CA 92037, USA
[9]National Center for Advancing Translational Sciences, National Institutes of Health, 9800 Medical Center Drive, Bethesda, MD 20892, USA
[10]Biochemistry and Molecular Biophysics Graduate Group, Perelman School of Medicine, University of Pennsylvania, Philadelphia, PA 19104, USA
[11]Department of Cell and Developmental Biology, Perelman School of Medicine, University of Pennsylvania, Philadelphia, PA 19104, USA
[12]Institute for Regenerative Medicine, Perelman School of Medicine, University of Pennsylvania, Philadelphia, PA 19104, USA
[13]The Epigenetics Institute, Perelman School of Medicine, University of Pennsylvania, Philadelphia, PA 19104, USA
[14]Department of Psychiatry, Perelman School of Medicine, University of Pennsylvania, Philadelphia, PA 19104, USA
[15]Lead Contact
*Correspondence: abang@sbpdiscovery.org (A.G.B.), shongjun@pennmedicine.upenn.edu (H.S.), juanct@scripps.edu (J.C.d.l.T.), gming@pennmedicine.upenn.edu (G.-l.M.)
https://doi.org/10.1016/j.stem.2020.09.016

SUMMARY

Neurological complications are common in patients with COVID-19. Although severe acute respiratory syndrome coronavirus 2 (SARS-CoV-2), the causal pathogen of COVID-19, has been detected in some patient brains, its ability to infect brain cells and impact their function is not well understood. Here, we investigated the susceptibility of human induced pluripotent stem cell (hiPSC)-derived monolayer brain cells and region-specific brain organoids to SARS-CoV-2 infection. We found that neurons and astrocytes were sparsely infected, but choroid plexus epithelial cells underwent robust infection. We optimized a protocol to generate choroid plexus organoids from hiPSCs and showed that productive SARS-CoV-2 infection of these organoids is associated with increased cell death and transcriptional dysregulation indicative of an inflammatory response and cellular function deficits. Together, our findings provide evidence for selective SARS-CoV-2 neurotropism and support the use of hiPSC-derived brain organoids as a platform to investigate SARS-CoV-2 infection susceptibility of brain cells, mechanisms of virus-induced brain dysfunction, and treatment strategies.

INTRODUCTION

Severe acute respiratory syndrome coronavirus 2 (SARS-CoV-2), the pathogen responsible for the COVID-19 pandemic, has infected over 34 million people and has contributed to over 1 million deaths worldwide by October 1st of this year (WHO, 2020). Although the disease primarily affects the respiratory system, damages and dysfunction have also been found in other organs, including the kidney, heart, liver, and brain (Yang et al.,

2020b). Neurological complications, such as cerebrovascular injury, altered mental status, encephalitis, encephalopathy, dizziness, headache, hypogeusia, and hyposmia, as well as neuropsychiatric ailments, including new onset psychosis, neurocognitive syndrome, and affective disorders, have been reported in a significant number of patients (Mao et al., 2020; Varatharaj et al., 2020). Viral RNA has been detected in the brain and cerebrospinal fluid (CSF) of some patients with COVID-19 and concomitant neurological symptoms (Helms et al., 2020;
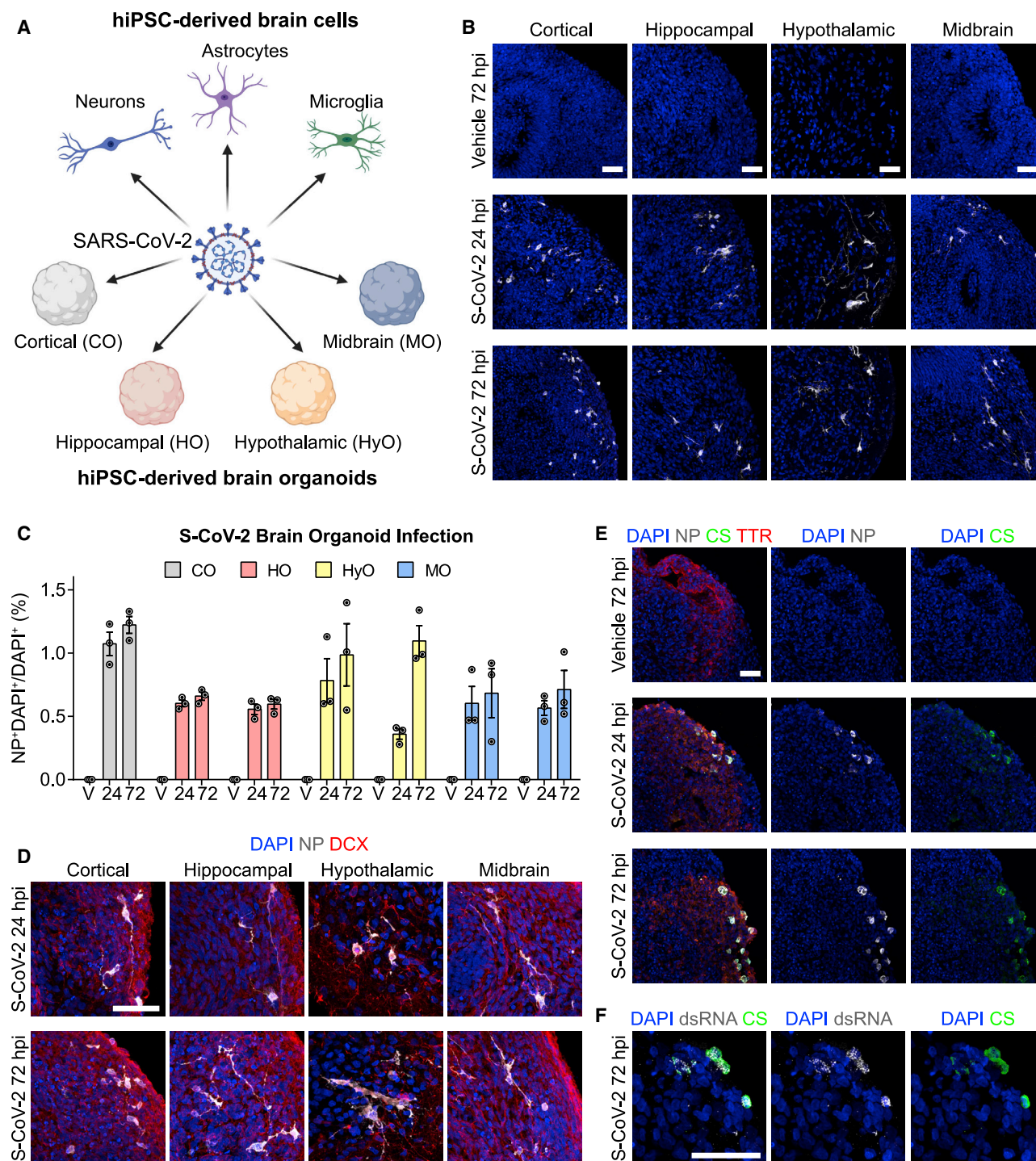
Figure 1. SARS-CoV-2 Neurotropism in hiPSC-Derived Brain Organoids

(A) Diagram outlining the strategy for testing the broad susceptibility of brain cells to SARS-CoV-2 infection. Tested cultures include hiPSC-derived cortical neurons, astrocytes, and microglia in monolayer cultures and hiPSC-derived cortical, hippocampal, hypothalamic, and midbrain organoids.

(B) Representative confocal images of fluorescent immunohistology for DAPI and SARS-CoV-2 nucleoprotein (NP) in hiPSC-derived cortical, hippocampal, hypothalamic, and midbrain organoids after SARS-CoV-2 (S-CoV-2) (10^5 FFUs) or vehicle treatment at 24 and 72 h post-infection (hpi). Scale bars, 50 μm. FFUs, focus-forming units.

(C) Quantification of percentages of NP$^+$DAPI$^+$ cells among DAPI$^+$ cells in S-CoV-2 (10^5 FFUs) and vehicle (V)-treated, hiPSC-derived cortical organoid (CO), hippocampal organoid (HO), hypothalamic organoid (HyO), and midbrain organoid (MO) cultures at 24 and 72 hpi. Values represent mean ± SEM with individual data points plotted (n = 3 organoids per brain region and condition with 3 images per organoid). Brain organoids derived from two independent hiPSC lines were analyzed for HO, HyO, and MO.

(legend continued on next page)

Cell Stem Cell
Short Article

CellPress

Moriguchi et al., 2020; Puelles et al., 2020; Solomon et al., 2020). Despite numerous reports of neurological findings in patients with COVID-19, it remains unclear whether these symptoms are a consequence of direct neural infection, para-infectious or post-infectious immune-mediated disease, or sequalae of systemic disease (Ellul et al., 2020; Iadecola et al., 2020). Variability in patient presentation and variable timing of testing for viral RNA in the CSF or brain complicate the interpretation of results in human patients. Limited availability of autopsy brain tissue from patients with COVID-19 and neurological symptoms and the inability to study ongoing disease pathogenesis in the human brain further underscore the need for accessible and tractable experimental models to investigate SARS-CoV-2 neurotropism, its functional impact, and to test therapeutics.

Classic animal models, such as rodents, are limited in their ability to recapitulate human COVID-19 symptoms and usually require viral or transgenic mediated overexpression of human SARS-CoV-2 receptor angiotensin-converting enzyme 2 (ACE2) to exhibit symptoms (Bao et al., 2020; Sun et al., 2020). Although cell lines, including many human cancer cell lines, have been used to study SARS-CoV-2 infection and test drug efficacy (Hoffmann et al., 2020b; Ou et al., 2020; Shang et al., 2020; Wang et al., 2020), they do not accurately recapitulate normal human cell behavior and often harbor tumor-associated mutations, such as TP53, which may affect SARS-CoV-2 replication or the cellular response to SARS-CoV-2 infection (Ma-Lauer et al., 2016). Furthermore, human tissue and organ systems contain multiple cell types with variable levels of ACE2 expression and viral susceptibility, which are not adequately represented in these human cell lines. These limitations support the development of human cellular models for SARS-CoV-2 infection that better recapitulates the cellular heterogeneity and function of individual tissues.

Human pluripotent stem cell (hiPSC)-based models provide an opportunity to investigate the susceptibility of various brain cell types to viral infection and their consequences. hiPSCs have been used to generate a variety of monolayer and three-dimensional (3D) organoid cultures to study human diseases and potential treatments. For example, hiPSC-derived neural progenitors in monolayer and brain organoids were instrumental in studying the impact of Zika virus (ZIKV) infection on human brain development and solidifying the link between ZIKV infection of neural progenitor cells and microcephaly seen in newborns (Ming et al., 2016; Qian et al., 2016; Tang et al., 2016). Additionally, these cultures were useful in screening for drugs to treat ZIKV infection (Xu et al., 2016). Recently, hiPSC-derived organoids have been used to model SARS-CoV-2 infection in many organs, including the intestine, lung, kidney, liver, pancreas, vasculature, and brain (Lamers et al., 2020; Monteil et al., 2020; Ramani et al., 2020; Yang et al., 2020a; Zhou et al., 2020). These studies have shown that SARS-CoV-2 can infect and replicate within cells of multiple organs, leading to transcriptional changes indicative of inflammatory responses and altered cellular functions. Here, we used hiPSC-derived neurons, astrocytes, and microglia in monolayer cultures and region-specific brain organoids of the cerebral cortex, hippocampus, hypothalamus, and midbrain to investigate the susceptibility of brain cells to SARS-CoV-2 infection. We observed sparse infection of neurons and astrocytes, with the exception of regions of organoids with choroid plexus epithelial cells that exhibited high levels of infectivity. Using an optimized protocol to generate choroid plexus organoids (CPOs) from hiPSCs, we showed evidence of productive infection by SARS-CoV-2 and functional consequences at cellular and molecular levels.

RESULTS

SARS-CoV-2 Neurotropism in Various hiPSC-Derived Brain Cells and Organoids

To investigate the susceptibility of human brain cells to SARS-CoV-2 infection, we tested various hiPSC-derived neural cells in monolayer cultures and region-specific brain organoids generated using several established (Qian et al., 2016, 2018) and modified protocols (Sakaguchi et al., 2015; Figure 1A). Monolayer hiPSC-derived cortical neurons, astrocytes, and microglia were exposed to either SARS-CoV-2 virus isolate or vehicle control for 12 h and analyzed at 24, 48, and 120 h post-infection (hpi) for immunolabeling using convalescent serum from a patient with COVID-19 or SARS-CoV-2 nucleoprotein antibodies (Figures S1A–S1C). We confirmed the identity of neurons, microglia, and astrocytes by immunostaining for markers MAP2, PU.1, and GFAP, respectively (Figures S1A–S1C). hiPSC-derived cortical neurons were co-cultured on hiPSC-derived astrocytes to improve survival, and analysis at 120 hpi showed rare infection of MAP2+ cells (Figure S1A). At 48 and 120 hpi, hiPSC-derived microglia showed no infection of PU.1+ cells (Figure S1B), whereas hiPSC-derived astrocytes showed sparse infection of GFAP+ cells (Figure S1C). As a validation, we tested infection of primary human astrocytes and observed sparse infection at 24, 48, and 120 hpi (Figure S1D). Quantification of hiPSC-derived and primary human astrocytes showed infection of 0.02% and 0.18% of all cells at 120 hpi, respectively (Figure S1E). These results revealed the ability of SARS-CoV-2 to infect monolayer human cortical neurons and astrocytes, but not microglia, although infection of neurons and astrocytes was rare.

To examine the neurotropism of SARS-CoV-2 in a model system that more closely resembles the human brain, we exposed hiPSC-derived cortical, hippocampal, hypothalamic, and midbrain organoids to SARS-CoV-2 or vehicle control for 8 h and analyzed samples at 24 and 72 hpi. We confirmed the

(D) Representative confocal images of fluorescent immunohistology for DAPI, NP, and neuronal marker doublecortin (DCX) in hiPSC-derived cortical, hippocampal, hypothalamic, and midbrain organoids after S-CoV-2 (10^5 FFUs) treatment at 24 and 72 hpi. Scale bar, 50 μm.

(E) Representative confocal images of fluorescent immunohistology for DAPI, NP, convalescent serum from a patient with COVID-19 (CS), and transthyretin (TTR) in hippocampal organoids after S-CoV-2 (10^5 FFUs) or vehicle treatment at 24 and 72 hpi, highlighting regions with choroid plexus cell differentiation. Scale bar, 50 μm.

(F) Representative confocal images of fluorescent immunohistology for DAPI, double-stranded RNA (dsRNA), and patient convalescent serum (CS) in a hippocampal organoid with a region of choroid plexus differentiation after S-CoV-2 (10^5 FFUs) treatment at 72 hpi. Scale bar, 50 μm.
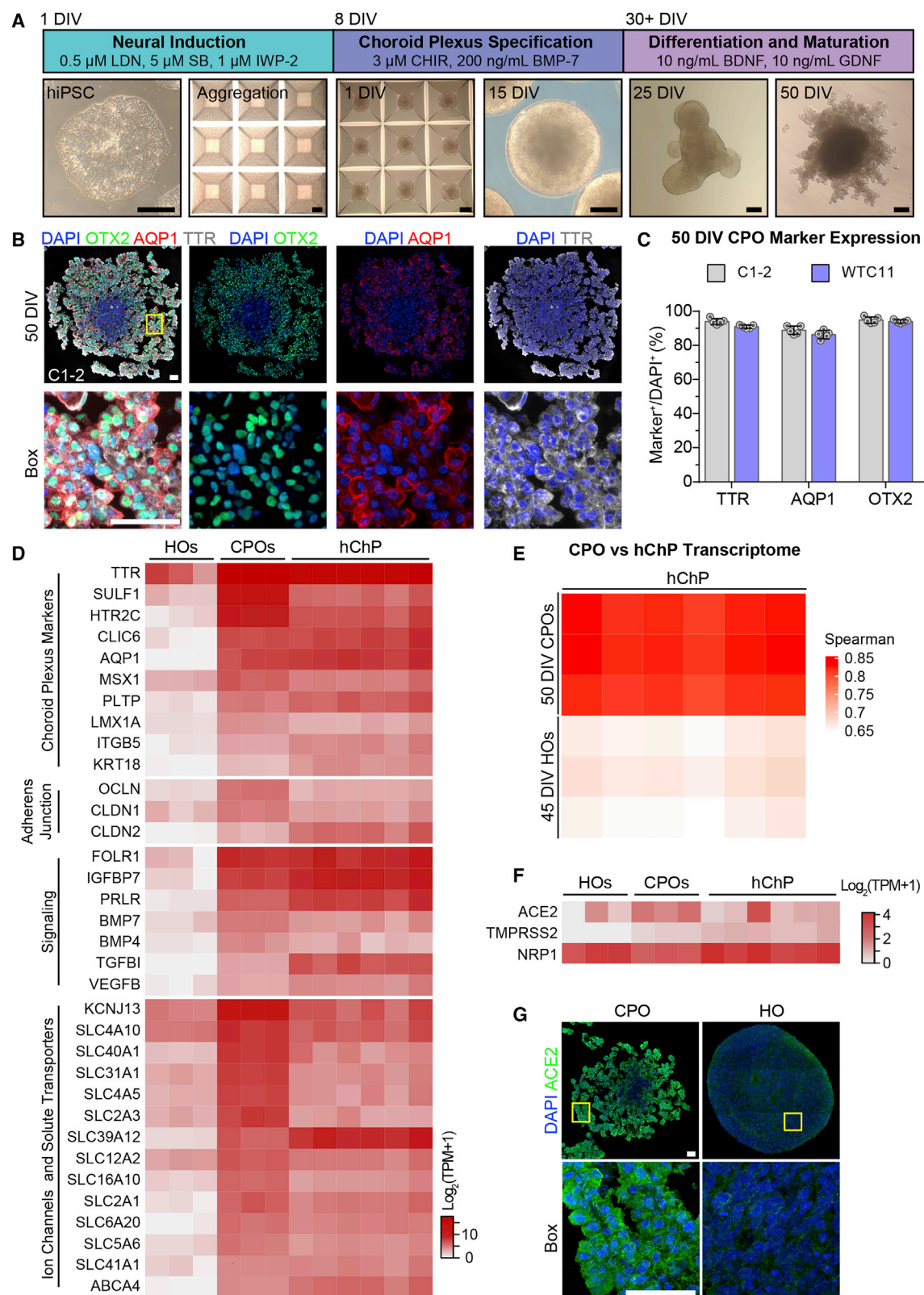Also see Figure S1.

Figure 2. Generation of Choroid Plexus Organoids from hiPSCs

(A) Diagram describing the protocol for generating choroid plexus organoids (CPOs) from hiPSCs with sample bright-field images of hiPSCs, aggregated hiPSCs, and CPOs at 1, 15, 25, and 50 days *in vitro* (DIV). Scale bars, 200 μm.

Cell Stem Cell
Short Article

CellPress

regional identity of cortical, hippocampal, hypothalamic, and midbrain organoids by immunostaining with the markers CTIP2, PROX1, OTP, and TH, respectively (Figure S1F). SARS-CoV-2 nucleoprotein was detected sparsely in these organoids derived from two different hiPSC lines in a range that averaged between 0.6% and 1.2% of all cells at 24 and 72 hpi (Figures 1B, 1C, and S1G). Co-immunolabeling with doublecortin (DCX) and SARS-CoV-2 nucleoprotein identified most of infected cells as neurons in all organoids (Figure 1D), and infection of some GFAP+ astrocytes was found in hypothalamic organoids (Figure S1H). Because these brain organoids contained mostly neurons, the relative susceptibility of neurons compared to astrocytes could not be assessed with certainty. The number of infected cells did not significantly increase from 24 to 72 hpi (Figure 1C), indicating that infection may not spread among neurons in brain organoids within this time window.

During development, the choroid plexus develops adjacent to the hippocampus (Lun et al., 2015) and some of our hippocampal organoids contained regions with choroid plexus epithelial cells, which were identified by transthyretin (TTR) expression (Figure 1E). Notably, we observed a greater density of infected cells in these regions (Figure 1E). Additionally, we observed co-localization of patient convalescent serum and double-stranded RNA (dsRNA) immunolabeling in regions with choroid plexus cells, further supporting SARS-CoV-2 infection (Figure 1F).

Together, these results demonstrate that SARS-CoV-2 exhibits limited tropism for neurons and astrocytes of multiple brain regions but higher infectivity of choroid plexus epithelial cells.

Generation of Choroid Plexus Organoids from hiPSCs

To validate the higher susceptibility and further investigate consequences of SARS-CoV-2 infection of choroid plexus cells, we sought to generate more pure choroid plexus organoids from hiPSCs. The most dorsal structures of the telencephalon, including the choroid plexus, are patterned by high WNT and BMP signaling from the roof plate (Lun et al., 2015). An early *in vitro* study demonstrated the sufficiency of BMP4 exposure to induce choroid plexus fate from neuroepithelial cells (Watanabe et al., 2012). Furthermore, exposure of human embryonic stem cell-derived embryoid bodies to the GSK3β antagonist CHIR-99021 and BMP4 was shown to generate 3D choroid plexus tissue (Sakaguchi et al., 2015). Building upon these previous studies, we optimized a simple protocol to generate choroid plexus organoids (CPOs) from hiPSCs (Figure 2A). Undifferentiated hiPSCs grown in a feeder-free condition were aggregated into embryoid bodies consisting of approximately 5,000 cells

each using an Aggrewell plate (Figure 2A). Embryoid bodies were patterned to the anterior neuroectodermal fate using dual-SMAD inhibition combined with WNT inhibition (Figure 2A). At 8 days *in vitro* (DIV), neural progenitors were patterned toward the choroid plexus fate by promoting high WNT signaling using the GSK3β antagonist CHIR-99021 and high levels of human recombinant BMP-7. CPOs maintained a round morphology at 15 DIV and expressed medial forebrain markers LMX1A and OTX2, with minimal numbers of FOXG1+ cells at 20 DIV, indicating choroid plexus progenitor fate (Figures S2A and S2B). CPOs began to form more translucent cellular extensions by 25 DIV that produce thinner projections lined by cuboidal cells by 50 DIV (Figure 2A). At 50 DIV, CPOs displayed morphology resembling the human choroid plexus epithelium with extensions of cuboidal epithelial cells expressing choroid plexus markers OTX2, aquaporin 1 (AQP1), and TTR (Figures 2B and S2C). Quantification of cells expressing various markers showed very high purity and consistency across two hiPSC lines (Figures 2C and S2B).

To further characterize these CPOs, we performed transcriptome analysis of CPOs at 50 DIV by bulk RNA sequencing (RNA-seq). Gene expression analysis confirmed the expression of choroid plexus markers, including TTR, AQP1, chloride intracellular channel 6 (CLIC6), keratin 18 (KRT18), MSX1, and LMX1A, in CPOs at high levels comparable to published transcriptomes of adult human choroid plexus tissue (Rodriguez-Lorenzo et al., 2020) and at much higher levels than those in hippocampal organoids at 45 DIV (Figure 2D). In addition, CPOs expressed genes related to adherens junction, signaling, ion channels, and solute transporters at high levels comparable to those in adult human choroid plexus tissue (Figure 2D), indicating choroid plexus identity and function. At the whole transcriptome level, CPOs, but not hippocampal organoids, showed high correlation to adult human choroid plexus tissue (Figure 2E). We validated high levels of expression of a group of choroid plexus signature genes in CPOs at 50 DIV and 100 DIV in comparison to hippocampal organoids at 20 DIV by qPCR (Figure S2D; Table S1).

Given our initial finding of a high rate of infection of choroid plexus cells by SARS-CoV-2, we examined the expression of known SARS-CoV-2 receptors. RNA-seq analysis showed expression of ACE2 and TMPRSS2 in CPOs at levels similar to the adult human choroid plexus tissue, which were much higher than in hippocampal organoids (Figure 2F). Expression levels of NRP1, a newly identified receptor for SARS-CoV-2 (Cantuti-Castelvetri et al., 2020), were similar in all three samples. Immunohistology confirmed expression of ACE2 at a much higher level in

(B) Representative confocal images of fluorescent immunohistology for DAPI, OTX2, AQP1, and TTR in CPOs at 50 DIV (made from C1-2 hiPSCs). Shown on the top panel are tiled images. Scale bars, 50 μm.

(C) Quantification of percentages of TTR+, AQP1+, and OTX2+ cells among DAPI+ cells in CPOs at 50 DIV. Values represent mean ± SEM with individual data points plotted (n = 5 organoids per hiPSC line with 3 images per organoid).

(D) Heatmap comparing expression of choroid plexus markers and genes related to adherens junction, cell signaling, and ion channel and solute transport genes within the bulk RNA transcriptomes of 45 DIV hippocampal organoids (HOs), 50 DIV CPOs, and adult human choroid plexus tissue (hChP) (Rodriguez-Lorenzo et al., 2020). Values are shown as Log2(TPM + 1).

(E) Heatmap comparing the Spearman correlation of the bulk RNA transcriptomes of 50 DIV CPOs and 45 DIV HOs to adult hChP (Rodriguez-Lorenzo et al., 2020).

(F) Heatmap comparing expression of SARS-CoV-2 receptor genes within the bulk RNA transcriptomes of 45 DIV HOs, 50 DIV CPOs, and hChP (Rodriguez-Lorenzo et al., 2020). Values are shown as Log2(TPM + 1).

(G) Representative confocal images of fluorescent immunohistology for DAPI and ACE2 in the 50 DIV CPO and 65 DIV HO (made from C1-2 hiPSCs). Shown on the top panel are tiled images. Scale bars, 50 μm.
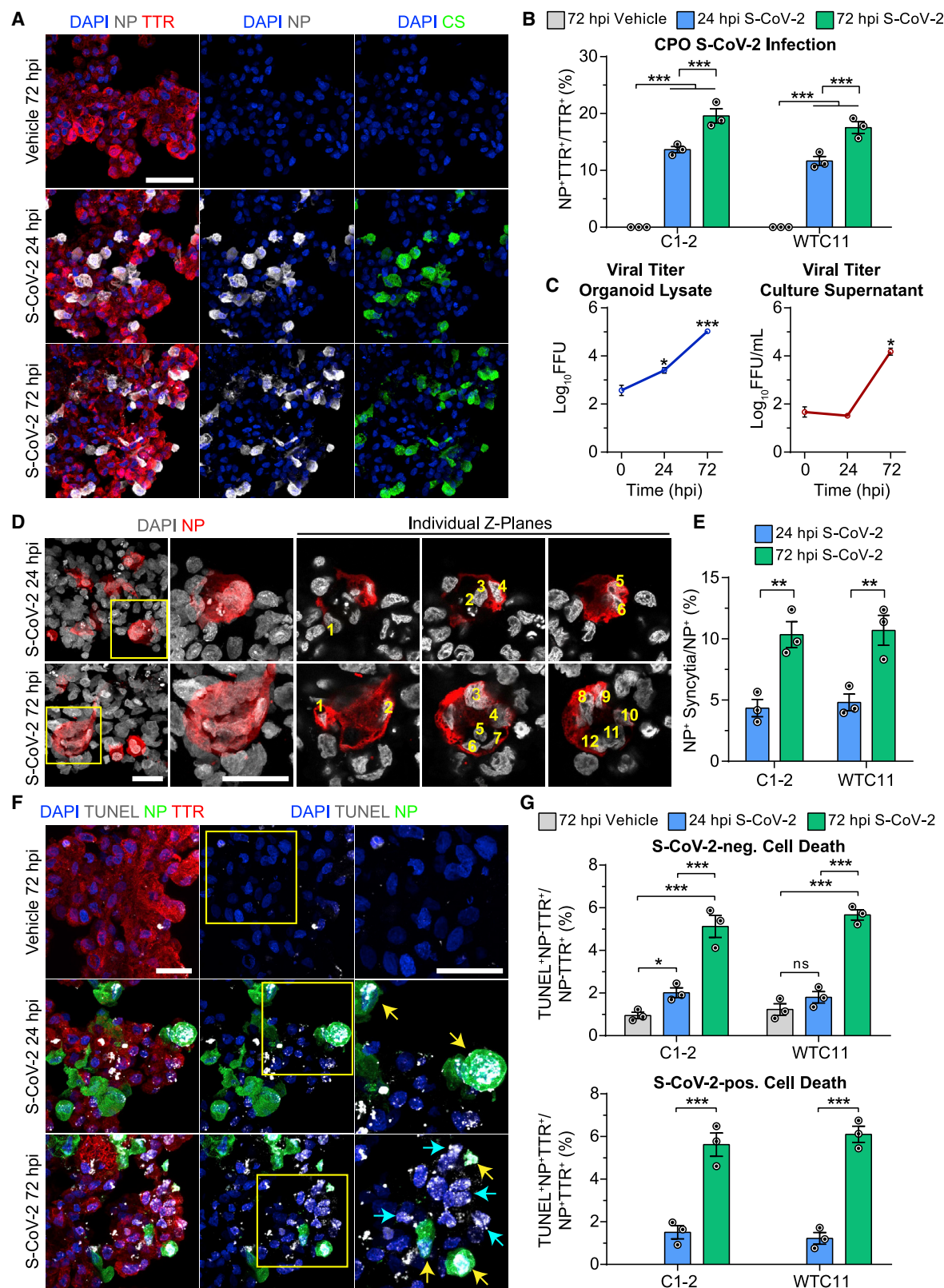
Also see Figure S2 and Table S1.

Figure 3. Productive Infection of Choroid Plexus Organoids and Increased Cell Death by SARS-CoV-2

(A) Representative confocal images of fluorescent immunohistology for DAPI, SARS-CoV-2 NP, patient CS, and TTR after S-CoV-2 (10^5 FFUs) or vehicle treatment of 67 DIV CPOs at 24 and 72 hpi. Scale bar, 50 μm.

(legend continued on next page)

Cell Stem Cell
Short Article

CellPress

CPOs than in hippocampal organoids (Figure 2G). qPCR analysis also showed higher levels of ACE2 and TMPRSS2 expression in CPOs at 50 DIV and 100 DIV than in hippocampal organoids (Figure S2D).

Together, these results show that our CPOs exhibit a similar transcriptome as adult human choroid plexus tissue and express markers for choroid plexus epithelial cells and SARS-CoV-2 receptors, representing a suitable experimental model to study SARS-CoV-2 infection.

Productive Infection of hiPSC-Derived Choroid Plexus Organoids by SARS-CoV-2 and Cellular Consequences

Next, we exposed CPOs at 47 DIV and 67 DIV to either SARS-CoV-2 or vehicle control for 8 h and analyzed samples at 24 and 72 hpi. Upon SARS-CoV-2, but not vehicle treatment, many TTR$^+$ choroid plexus cells showed infection as identified by co-localization of patient convalescent serum and SARS-CoV-2 nucleoprotein immunolabeling in CPOs derived from two independent hiPSC lines (Figures 3A and S3A). Additionally, we observed co-localization of patient convalescent serum and abundant dsRNA immunolabeling in TTR$^+$ choroid plexus cells (Figure S3B). Infected cells identified by SARS-CoV-2 nucleoprotein immunostaining also showed high levels of ACE2 expression, consistent with ACE2 being a critical cell entry receptor for SARS-CoV-2 (Figure S3C). Quantification revealed an average of 9.0% and 12.6% of TTR$^+$ cells infected at 24 hpi and 11.9% and 18.6% of TTR$^+$ cells infected at 72 hpi for CPOs infected at 47 DIV and 67 DIV, respectively, across two hiPSC lines (Figures 3B and S3D). An increase in the number of infected cells from 24 to 72 hpi suggested that infection could be productive and spread among cells (Figures 3B and S3D). To confirm SARS-CoV-2 productive infection, we examined viral titers using culture supernatants and CPO lysates at 0, 24, and 72 hpi. There was a significant increase in titers of infectious virus over time after the initial infection (Figure 3C). The increase of infectious virus present in CPO lysates superseded the increase in culture supernatants, suggesting a slow release of infectious viruses into the culture medium. The increase in viral titers appeared to be bigger than the increase in the number of infected cells, suggesting that the relationship is not linear. Consistent with this notion, exposure of CPOs at 67 DIV to different amounts of SARS-CoV-2 showed a non-linear increase in infection with higher viral titers (Figures S3E and S3F). Importantly, we observed infection using 10^3 FFUs (focus-forming units) with an estimated MOI (multiplic-

ity of infection) of 0.001, indicating very high susceptibility of CPOs to SARS-CoV-2 infection (Figures S3E and S3F).

Next, we examined the cellular consequence of SARS-CoV-2 infection of CPOs. We observed the presence of syncytia in SARS-CoV-2-infected cells, which significantly increased from an average of 4.6% at 24 hpi to 10.5% by 72 hpi (Figures 3D and 3E). Development of syncytia by cell-cell fusion mediated by interaction between SARS-CoV-2 spike protein and ACE2 expressed on adjacent cells has been reported with SARS-CoV-2 infection of several cell types and is a major mechanism for viral spread (Hoffmann et al., 2020a; Matsuyama et al., 2020; Ou et al., 2020). In particular, the SARS-CoV-2 spike protein appears to facilitate membrane fusion at a much higher rate than SARS-CoV-1 (Xia et al., 2020). By examining individual confocal Z-planes, we could identify as many as 12 nuclei within a single infected cell at 72 hpi (Figure 3D). Interestingly, in addition to syncytia, we observed a significant increase in cell death in both infected and uninfected TTR$^+$ choroid plexus cells in CPOs exposed to SARS-CoV-2 as measured by TUNEL immunolabeling (Figures 3F, 3G, and S3G). Cell death increased from an average of 1.4% to 5.9% in infected and from 1.9% to 5.4% in uninfected TTR$^+$ cells from 24 to 72 hpi in CPOs infected at 67 DIV across two hiPSC lines (Figure 3G). TUNEL$^+$ uninfected cells tended to appear adjacent to infected cells, suggesting that infected cells may induce adjacent cells to die through an extrinsic mechanism (Figure 3F). Similar results were found for CPOs infected at 47 DIV (Figure S3G).

To confirm the susceptibility of choroid plexus epithelial cells to SARS-CoV-2 infection, we examined primary human choroid plexus epithelial cells (pHCPECs). pHCPECs exposed to SARS-CoV-2, but not vehicle control, for 12 h showed many infected cells by immunolabeling with SARS-CoV-2 nucleoprotein at 72 and 120 hpi (Figure S3H). The number of infected cells increased with higher MOI, with an average of 1.7% and 0.9% of cells infected at 72 and 120 hpi, respectively, using a MOI of 5 (Figure S3I).

Together, using CPOs as a 3D human cellular model, our findings reveal SARS-CoV-2 tropism for choroid plexus epithelial cells that results in productive infection, increased cell syncytia that may promote viral spread through cell-cell fusion, and increased cell death among both infected and uninfected adjacent cells.

Transcriptional Dysregulation of Choroid Plexus Organoids upon SARS-CoV-2 Infection

To gain additional insight into functional consequences of SARS-CoV-2 infection in CPOs at the molecular level, we performed

---

(B) Quantification of percentages of NP$^+$TTR$^+$ cells among TTR$^+$ cells after S-CoV-2 (10^5 FFUs) or vehicle treatment of 67 DIV CPOs at 24 and 72 hpi. Values represent mean ± SEM with individual data points plotted (n = 3 organoids per hiPSC line with 3 images per organoid; ***p < 0.001; Fisher's least significant difference [LSD] test).

(C) Quantification of viral titers from CPO lysates (left) and culture supernatants (right) after S-CoV-2 (10^5 FFUs) treatment of 47 DIV CPOs at 0, 24, and 72 hpi. Values represent mean ± SD (n = 2 biological replicates consisting of 4 organoids each; *p < 0.05; ***p < 0.001; Student's t test).

(D) Representative confocal images of fluorescent immunohistology for DAPI and NP after S-CoV-2 (10^5 FFUs) treatment of 47 DIV CPOs at 24 and 72 hpi. Boxed regions show NP$^+$ syncytia with individual Z-planes separated to highlight multiple nuclei counted within each syncytium. Scale bars, 25 μm.

(E) Quantification of the percentages of NP$^+$ syncytia among total NP$^+$ cells after S-CoV-2 (10^5 FFUs) treatment of 47 DIV CPOs at 24 and 72 hpi. Values represent mean ± SEM with individual data points plotted (n = 3 organoids per hiPSC line with 3 images per organoid; **p < 0.01; Fisher's LSD test).

(F) Representative confocal images of fluorescent immunohistology for DAPI, TUNEL, NP, and TTR after S-CoV-2 (10^5 FFUs) or vehicle treatment of 67 DIV CPOs at 24 and 72 hpi. Boxed regions highlight NP$^+$TUNEL$^+$ cells. Yellow arrows highlight NP$^-$TUNEL$^+$ cells near NP$^+$ cells. Scale bars, 25 μm.

(G) Quantification of percentages of TUNEL$^+$NP$^-$TTR$^+$ cells among NP$^-$TTR$^+$ cells (top) and TUNEL$^+$NP$^+$TTR$^+$ cells among NP$^+$TTR$^+$ cells (bottom) after S-CoV-2 (10^5 FFUs) or vehicle treatment of 67 DIV CPOs at 24 and 72 hpi. Values represent mean ± SEM with individual data points plotted (n = 3 organoids per hiPSC line with 3 images per organoid; *p < 0.05; ***p < 0.001; ns, not significant, p > 0.05; Fisher's LSD test).

Also see Figure S3.

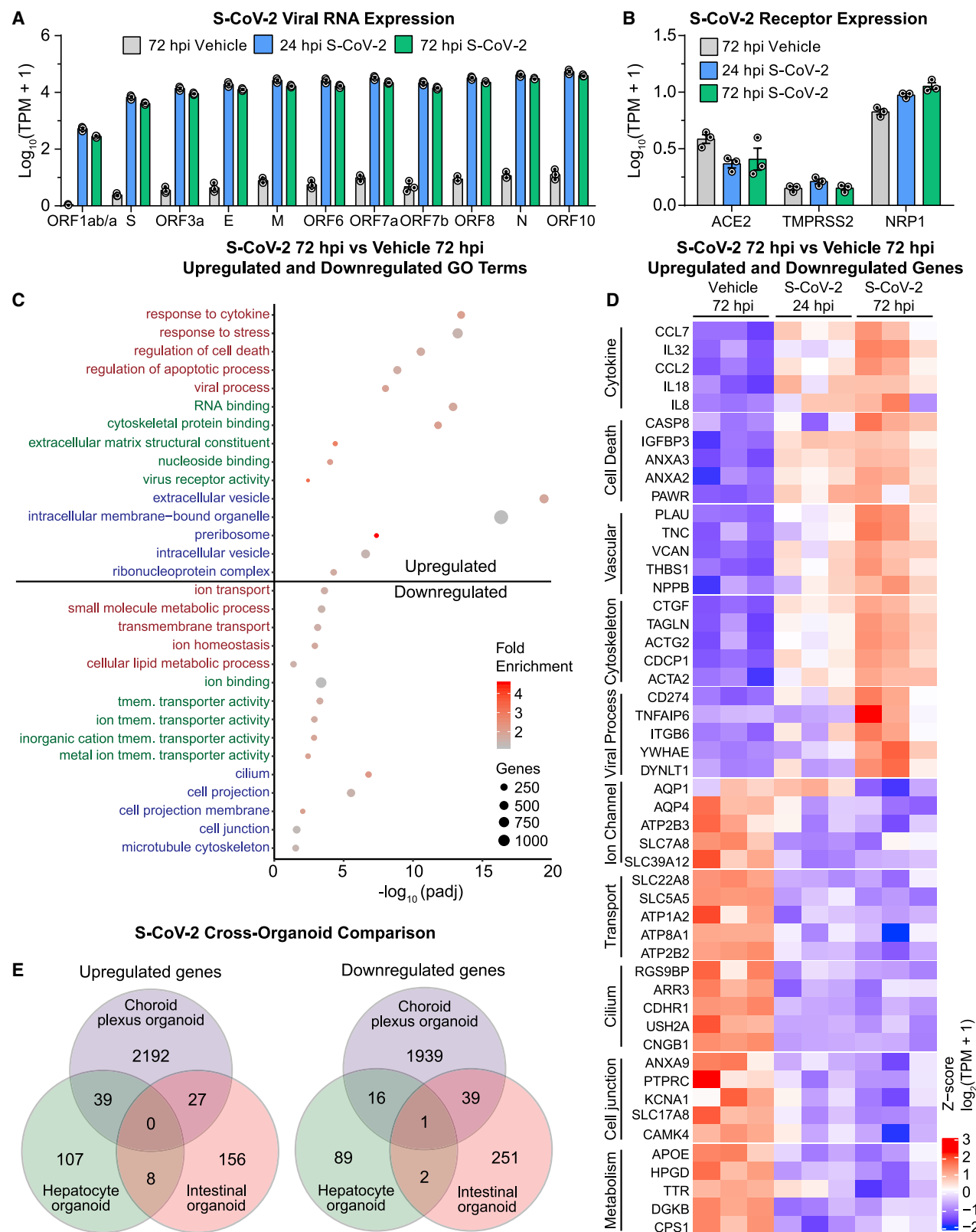**Figure 4. Transcriptional Dysregulation in Choroid Plexus Organoids upon SARS-CoV-2 Infection**

(A) Quantification comparing $\text{Log}_{10}(\text{TPM}+1)$ of S-CoV-2 viral transcripts after S-CoV-2 (10^5 FFUs) or vehicle treatment of 47 DIV CPOs at 24 and 72 hpi by bulk RNA-seq. Values represent mean ± SEM with individual data points plotted (n = 3 biological replicates containing 3 organoids each).

Cell Stem Cell
Short Article

CellPress

RNA-seq of SARS-CoV-2 and vehicle-treated 47 DIV CPOs at 24 and 72 hpi. Principal-component analysis showed clustering of biological replicates within different treatment groups (Figure S4A). After aligning reads to the SARS-CoV-2 genome, we detected high numbers of viral transcripts at 24 and 72 hpi, confirming that the virus was replicating within CPOs (Figure 4A). We also confirmed the expression of SARS-CoV-2 receptors ACE2, TMPRSS2, and NRP1 in CPOs at all time points (Figure 4B). Comparison of SARS-CoV-2 and vehicle-treated CPOs revealed 1,721 upregulated genes and 1,487 downregulated genes at 72 hpi, indicating that SARS-CoV-2 infection leads to large-scale transcriptional dysregulation (Figure S4B; Table S2).

More detailed gene ontology (GO) analysis of upregulated genes at 72 hpi showed enrichment for genes related to viral responses, RNA processing, response to cytokine, cytoskeletal rearrangement, and cell death (Figure 4C; Table S3). Closer examination of upregulated genes revealed an increase in inflammatory cytokines CCL7, interleukin-32 (IL-32), CCL2 (MCP1), IL-18, and IL-8 (Figure 4D). IL-32 plays important roles in both innate and adaptive immune responses by inducing tumor necrosis factor alpha (TNF-α), which activates the signaling pathway of nuclear factor κB (NF-κB) and p38 mitogen-activated protein kinase (MAPK). This signaling pathway has been shown to be activated following SARS-CoV-2 infection in other cells (Bouhaddou et al., 2020). We validated the upregulation of p38 signaling by immunostaining of the phosphorylated form of p38 in infected cells (Figures S4C and S4D). Interestingly, quantification showed elevated levels of phospho-p38 in nearby uninfected cells, although to a lesser degree than in infected cells, suggesting a substantial non-cell-autonomous effect (Figure S4D). Upregulation of many vascular remodeling genes (Figure 4D), such as NPPB and VCAN, suggests that infected choroid plexus cells could signal the vasculature to promote leukocyte invasion (Shechter et al., 2013).

GO analysis of downregulated genes at 72 hpi, on the other hand, showed enrichment for genes related to ion transport, transmembrane transport, cilium, and cell junction (Figure 4C; Table S3). Closer examination of downregulated genes revealed a decrease in the expression of many transporters and ion channels, such as AQP1, AQP4, and SLC22A8, which are important for normal CSF secretory function (Figure 4D; Brown et al., 2004; Hladky and Barrand, 2016), suggesting functional deficits of choroid plexus cells. Downregulation of many cell junction genes suggests a remodeling or breakdown of normal CSF-blood barrier function, which also occurs during brain inflammation (Engelhardt and Tietz, 2015). Additionally, the dramatic decrease in TTR production may result in decreased thyroxine

transport to the CSF, which has been shown to contribute to neuropsychiatric symptoms and "brain fog" or difficulty in concentrating in patients (Samuels, 2014). We validated downregulation of TTR levels in infected cells by immunostaining (Figures S4C and S4D). We also observed downregulation of TTR levels in uninfected cells at 72 hpi, although to a lesser degree than in infected cells, again suggesting a non-cell-autonomous effect (Figure S4D).

Transcriptional dysregulation induced by SARS-CoV-2 in CPOs at 24 hpi showed similar gene expression changes as at 72 hpi, although less severe in most cases (Figures 4D and S4E). Comparison of the list of dysregulated genes at 24 and 72 hpi revealed a substantial overlap of 42% and 32% of upregulated and downregulated genes, respectively (Figure S4F). We validated the dysregulation of a subset of these genes by qPCR (Figure S4G).

To investigate whether organoids from different tissues exhibit similar transcriptional responses upon SARS-CoV-2 infection, we compared SARS-CoV-2-induced transcriptional changes among CPOs and published datasets from hepatocyte organoids (Yang et al., 2020a) and intestinal organoids (Lamers et al., 2020). Surprisingly, we found little overlap among upregulated or downregulated genes in the three different organoid types, suggesting a predominantly cell-type-specific response to SARS-CoV-2 infection (Figure 4E). This finding supports the use of a diverse array of human model systems to investigate effects of SARS-CoV-2 infection. Additionally, we found many more dysregulated genes in CPOs compared to the other two organoid types, suggesting that SARS-CoV-2 may exhibit a greater impact on choroid plexus cells (Figure 4E).

Together, these transcriptome analyses suggest that SARS-CoV-2 infection of choroid plexus cells leads to viral RNA production and inflammatory cellular responses with a concomitant compromise of normal barrier and secretory functions as well as increased cell death. Furthermore, responses to SARS-CoV-2 infection are largely tissue organoid specific, at least at the transcriptional level.

DISCUSSION

Using a platform of hiPSC-derived monolayer neurons, microglia, astrocytes, and region-specific brain organoids, we showed limited tropism of SARS-CoV-2 for neurons and astrocytes with a particularly high rate of infection of choroid plexus epithelial cells. Using an optimized protocol for generating CPOs from hiPSCs that resemble the morphology, marker expression, and transcriptome of adult human choroid plexus, we revealed

(B) Quantification comparing $Log_{10}(TPM+1)$ of known S-CoV-2 receptor transcripts after S-CoV-2 (10^5 FFUs) or vehicle treatment of 47 DIV CPOs at 24 and 72 hpi by bulk RNA-seq. Values represent mean ± SEM with individual data points plotted (n = 3 biological replicates containing 3 organoids each).

(C) Dot plot of selected enriched gene ontology (GO) terms for biological process (red), molecular function (green), and cellular component (blue) for upregulated and downregulated genes when comparing S-CoV-2 (10^5 FFUs) and vehicle-treated 47 DIV CPOs at 72 hpi. See Table S2 for the complete list of differentially expressed genes and Table S3 for the complete list of GO terms for differentially expressed genes. tmem., transmembrane.

(D) Heatmap of selected upregulated and downregulated genes when comparing S-CoV-2 (10^5 FFUs) and vehicle-treated 47 DIV CPOs at 72 hpi. Genes related to different biological functions are grouped and labeled. Values are shown for each biological replicate as the row Z score per gene of $Log_2(TPM+1)$-transformed values.

(E) Venn diagrams comparing the overlap of upregulated and downregulated genes following S-CoV-2 infection in CPOs, human hepatocyte organoids (Yang et al., 2020a), and human intestinal organoids (Lamers et al., 2020). Differentially expressed genes at both 24 and 72 hpi were combined for CPOs, and differentially expressed genes for both expansion and differentiation intestinal organoid types were combined for intestinal organoids.

Also see Figure S4 and Tables S1, S2, and S3.

productive infection of SARS-CoV-2 in choroid plexus epithelial cells, which we confirmed using primary human choroid plexus epithelial cells. Analysis of the consequence of SARS-CoV-2 infection of CPOs showed an increase in both cell-autonomous and non-cell-autonomous cell death and transcriptional dysregulation related to increased inflammation and altered barrier and secretory function. Our study provides an organoid platform to investigate the cellular susceptibility, pathogenesis, and treatment strategies of SARS-CoV-2 infection of brain cells and further implicates the choroid plexus as a potentially important site for pathophysiology. Notably, the choroid plexus is known to be a site of infection for several viruses and agents that affect the brain (Schwerk et al., 2015).

Modeling SARS-CoV-2 Infection with Brain Organoids

Although COVID-19 primarily manifests as respiratory distress resulting from inflammatory damage to the lung epithelium, there is mounting clinical evidence implicating other organs, such as the kidney, intestine, and brain, in disease pathogenesis (Renu et al., 2020). The currently widely used cellular model systems, such as Vero E6 cells or human cancer cell lines, do not adequately recapitulate the cellular diversity and breadth of the disease. Although mice engineered to express human ACE2 have provided an *in vivo* model to study SARS-CoV-2, the system relies on human ACE2 overexpression and does not fully recapitulate symptoms of COVID-19 in humans. Recently, organoids have emerged as a model to study human cells and organogenesis *in vitro* (Clevers, 2016). Organoids for various tissues have been used to better understand SARS-CoV-2 viral tropism and pathology (Lamers et al., 2020; Monteil et al., 2020; Ramani et al., 2020; Yang et al., 2020a; Zhou et al., 2020). These studies support cell-type-specific susceptibility to SARS-CoV-2 infection. Our finding that dysregulated gene expression varies widely among hepatocyte, intestinal, and choroid plexus organoids infected with SARS-CoV-2 suggests unique responses in different cell types and highlights the need for diverse human cellular model systems when studying the disease. Brain organoid models for SARS-CoV-2 infection are particularly useful because it is not feasible to take brain biopsies from patients with COVID-19. The load of SARS-CoV-2 that may enter the brain is likely to be variable throughout the course of illness and may be difficult to accurately assess in brain samples. For example, viral particles or RNA has been detected in the CSF or brain of some, but not the majority of, patients with neurological symptoms (Helms et al., 2020; Moriguchi et al., 2020; Puelles et al., 2020; Solomon et al., 2020; Virani et al., 2020), although the amount of viral particles in the CSF may be insufficient for detection (Ye et al., 2020). Brain organoids allow analyses of the acute and long-term impact of SARS-CoV-2 infection in real time, with the ability to introduce perturbations, such as therapeutic agents, to assess cellular responses. Use of region-specific brain organoids, including CPOs, expands the organoid toolset for investigating SARS-CoV-2 infection and provides a platform for testing new therapeutics.

Building upon previous findings (Sakaguchi et al., 2015; Watanabe et al., 2012), we optimized a CPO model that is simple, robust, and reproducible with the initial goal to study SARS-CoV-2 infection. These CPOs express high levels of SARS-CoV-2 receptors and exhibit productive infection of SARS-

CoV-2 and pathogenesis at cellular and molecular levels. CPOs may provide a better model system than primary human choroid plexus epithelial cells, which are not widely available and often lose some characteristics upon multiple rounds of expansion in culture and showed a lower infection rate than our CPOs. Unlike a very recently developed protocol that utilizes cultures with Matrigel extracellular matrix (Pellegrini et al., 2020), our CPOs do not obviously polarize or develop fluid-filled, cystic structures but do offer the benefit of not relying on Matrigel, which has batch-to-batch variation and can lead to increased inter-organoid variability. Our protocol uses feeder-free hiPSCs to further improve organoid reproducibility, and CPOs are cultured on an orbital shaker to enhance oxygen and nutrient diffusion throughout the organoids. With these improvements, CPOs reproducibly generate projections of cuboidal cells and exhibit uniform expression of choroid plexus markers OTX2, AQP1, and TTR in most of the cells within the organoids. They also exhibit a transcriptome similar to adult human choroid plexus tissue. Importantly, these CPOs express many transporters that are essential for CSF secretion. These CPOs provide a platform for future investigations of cell-type-specific pathogenesis, mechanisms, and treatment of SARS-CoV-2 infection. Our CPO platform can also be used to model human choroid plexus development and associated brain disorders in the future (Lun et al., 2015).

Neurotropism of SARS-CoV-2 and Choroid Plexus as a Potential Site for Viral Entry and Spread in the Central Nervous System

ACE2 has been identified as a key cell entry receptor for SARS-CoV-2 (Hoffmann et al., 2020b). Although moderate ACE2 expression has been detected in various brain regions, particularly high levels have been reported in the choroid plexus in humans and mice (Chen et al., 2020). The high levels of ACE2 expression in CPOs may explain their higher susceptibility to SARS-CoV-2 infection compared to other brain organoids. Moreover, the productive infection and high incidence of syncytia in infected choroid plexus cells may contribute to the viral spread. On the other hand, despite relatively low levels of ACE2 expression, we did detect sparse infection of neurons by SARS-CoV-2. Recent studies point to the potential for other proteins that are expressed more highly in neural cells, such as NRP1, to serve as receptors for SARS-CoV-2. We did not observe an obvious increase in the number of infected neurons over time, suggesting that the virus may not spread efficiently from neuron to neuron.

Central nervous system disorders, including seizures and encephalopathy, have been reported with SARS-CoV-1 with detection of infectious virus and RNA in the CSF (Hung et al., 2003; Lau et al., 2004; Xu et al., 2005). A substantial portion of patients with COVID-19 exhibit various neurological symptoms, which are highly variable, probably due to many factors (Helms et al., 2020; Moriguchi et al., 2020; Puelles et al., 2020; Solomon et al., 2020; Virani et al., 2020). How SARS-CoV-2 may enter the brain is currently unknown. The main hypotheses are either neuron-to-neuron spread via bipolar cells located in the olfactory epithelium that extend axons and dendrites to the olfactory bulb or a hematogenous route across the blood-CSF barrier (Desforges et al., 2014). Neuron-to-neuron propagation has been

Cell Stem Cell
Short Article

CellPress

described for other coronaviruses (Dubé et al., 2018; Netland et al., 2008), but it was not obvious in our study. Our finding that the choroid plexus is particularly susceptible to productive infection with SARS-CoV-2 raises the possibility that choroid plexus epithelial cells could be infected from virus circulating in closely associated capillaries. SARS-CoV-2 may replicate within choroid plexus cells and shed viral copies into the CSF. Indeed, we detected increased viral load in culture supernatants over time. Alternatively, virus may enter the CSF via the cribiform plate in nasal passages and then replicate in choroid plexus cells, increasing viral availability in the central nervous system. Viral propagation through the CSF may also explain cases of spinal cord pathology in some patients with COVID-19 (Giorgianni et al., 2020; Valiuddin et al., 2020). More-detailed analyses of autopsy brain samples from patients with COVID-19 and better animal models of SARS-CoV-2 infection are necessary to understand potential routes of viral entry into the brain.

Potential Role of the Choroid Plexus in SARS-CoV-2 Pathogenesis

The transcriptional dysregulation in CPOs after SARS-CoV-2 infection indicates an inflammatory response and perturbed choroid plexus cellular function. Our study further suggested both cell-autonomous and non-cell-autonomous impact of SARS-CoV-2 infection. Many pro-inflammatory cytokines were upregulated, including CCL7, IL-32, CCL2, IL-18, and IL-8, which are important for recruiting immune cells to sites of infection. Future studies are needed to validate the release of these cytokines by ELISA analyses. Notably, one case report examining inflammatory cytokines present in the serum and CSF of a patient with COVID-19 presenting with severe seizures identified CCL2 as the only cytokine enriched in the patient's CSF compared to serum (Farhadian et al., 2020). CCL2 was one of the most highly upregulated genes after SARS-CoV-2 infection, suggesting that the choroid plexus may be the source of this cytokine in the CSF. Upregulation of vascular and extracellular matrix remodeling genes also suggests that, during infection, choroid plexus cells can signal the adjacent vasculature to recruit inflammatory cells. Downregulation of many genes important for CSF secretion, including AQP1, and many ion transporters, such as ATP1A2, may lead to altered CSF production and composition. Mutations in many of these dysregulated transporter genes have been implicated in neurological complications in humans, such as migraine and encephalopathy (Murphy et al., 2018). Increased expression of cell death genes supports our finding of increased numbers of TUNEL^{+} cells after SARS-CoV-2 infection. Increased cell death and downregulation of cell junction genes, such as CLDN2, suggest damage to tight junctions between choroid plexus epithelial cells, which may disturb the blood-CSF barrier, allowing pathogens and regulated solutes to pass more freely (Ghersi-Egea et al., 2018). Downregulation of many genes related to the cilium suggests an impaired cytoskeleton and dysfunctional sensing of the extracellular environment. There was also a significant downregulation of TTR, which is necessary for carrying thyroid hormone from the blood into the CSF, and lowered TTR production by the choroid plexus has been associated with neuropsychiatric disorders, such as schizophrenia and depression (Huang et al., 2006; Sullivan

et al., 1999). Furthermore, low CSF thyroid hormone has been associated with many neurological symptoms, including slowing of thought and speech, decreased attentiveness, and reduced cognition, which have all been reported by patients with COVID-19 (Ellul et al., 2020). Our study implicates the choroid plexus epithelium as a potential target of SARS-CoV-2 infection and a contributor to COVID-19 disease pathogenesis that warrants further investigation.

Limitations of Study

Our study demonstrates clear susceptibility of hiPSC-derived neurons, astrocytes, and choroid plexus cells, as well as primary astrocytes and choroid plexus epithelial cells, to SARS-CoV-2 infection *in vitro*; however, a thorough analysis of brain samples from patients with COVID-19 is necessary to confirm neural susceptibility *in vivo*. Our methodology has a number of constraints that limit result interpretation. First, because brain organoids more closely resemble the developing fetal brain than the mature adult brain, there may exist important differences in SARS-CoV-2 susceptibility between immature and mature cells. There has been recent evidence of vertical transmission of SARS-CoV-2 from mother to fetus (Dong et al., 2020; Vivanti et al., 2020; Zeng et al., 2020), but the impact on the fetal brain remains unclear. Brain organoids may serve as a useful model system to explore the potential effects of fetal SARS-CoV-2 exposure on brain development. Second, direct exposure of brain organoid cultures to SARS-CoV-2 in the culture medium may not accurately recapitulate the physiological amount and duration of viral exposure in humans. Different viral titers may also reveal different viral tropism *in vitro*. To avoid the use of high titers that may cause non-physiological viral infection, we exposed different brain-region-specific organoids of the same estimated MOI of 0.1 and found a differential infection rate. Importantly, SARS-CoV-2 at an estimated MOI as low as 0.001 can lead to detectable infection of CPOs, indicating very high susceptibility of choroid plexus cells, at least *in vitro*. Third, brain organoid models lack an intact blood-brain barrier or blood-CSF barrier, which may modulate SARS-CoV-2 access to the brain. Our brain organoids also lack additional cell types, such as oligodendrocytes, microglia, stromal cells, immune cells, and endothelial cells, which may modulate susceptibility to infection and contribute to disease pathogenesis *in vivo*. Immune cells, such as T cells and monocytes, have been shown to mediate host responses to SARS-CoV-2 infection, including tissue-specific inflammation (Tay et al., 2020). Endothelial cells are major targets of SARS-CoV-2 and may be the primary cause of SARS-CoV-2-related effects in the brain with neurological symptoms being secondary to vascular changes and hypoxia (Ellul et al., 2020). Future studies of SARS-CoV-2 susceptibility can extend to a more-diverse selection of brain cells, as well as peripheral neurons.

It is currently unclear whether neurological symptoms present in patients with COVID-19 are a direct result of neural infection or secondary to endothelial cell damage and hypoxia, circulating pro-inflammatory cytokines, or ambulatory treatment. Further studies of patients will be necessary to better correlate the onset and severity of neurological symptoms with neural cell infection. Our *in vitro* studies provide useful information about specific cell types to focus on for future human studies and offers a simple, accessible, and tractable human cell platform to investigate

cellular susceptibility, disease mechanisms, and treatment strategies for SARS-CoV-2 infection of the human brain.

STAR★METHODS

Detailed methods are provided in the online version of this paper and include the following:

- KEY RESOURCES TABLE
- RESOURCE AVAILABILITY
  - Lead Contact
  - Materials Availability
  - Data and Code Availability
- EXPERIMENTAL MODEL AND SUBJECT DETAILS
  - Human Induced Pluripotent Stem Cells and Convalescent Serum from a Patient with COVID-19
- METHOD DETAILS
  - Monolayer Neural Cell Cultures
  - Human Induced Pluripotent Stem Cell Culture
  - Brain Organoid Cultures
  - Choroid Plexus Organoid Culture
  - SARS-CoV-2 Infection of Cultures
  - Tissue Processing and Immunohistology
  - Confocal Microscopy and Image Processing
  - Viral Titer Assay
  - RNA Isolation, Library Preparation, and Sequencing
  - Bioinformatics Analyses
  - Quantitative PCR Validation
- QUANTIFICATION AND STATISTICAL ANALYSIS

SUPPLEMENTAL INFORMATION

Supplemental Information can be found online at https://doi.org/10.1016/j.stem.2020.09.016.

AUTHOR CONTRIBUTIONS

F.J. contributed to histological analysis of various brain organoids and development of the CPO model. S.R.P. and F.Z. contributed to RNA-seq data analysis. F.Z. contributed to qPCR validation. W.-K.H. and S.Z.H.W. performed hypothalamic organoid analysis. F.Z. and D.Y.Z. performed RNA-seq. H.Z. contributed to monolayer cell culture, immunocytochemistry, and analyses. B.C. contributed to preparation of viral-infected samples and viral titer analysis. W.F. contributed to organoid cultures. C.Z.C., M.X., M.P., and W.Z. contributed to midbrain organoid generation. J.C.d.l.T. performed viral infection. W.Z., A.G.B., H.S., J.C.d.l.T., and G.M. conceived and guided the project. F.J., H.S., and G.M. wrote the manuscript with input from all authors.

DECLARATION OF INTERESTS

The authors declare no competing interests.

REFERENCES

Ashburner, M., Ball, C.A., Blake, J.A., Botstein, D., Butler, H., Cherry, J.M., Davis, A.P., Dolinski, K., Dwight, S.S., Eppig, J.T., et al. (2000). Gene ontology: tool for the unification of biology. The Gene Ontology Consortium. Nat. Genet. 25, 25–29.

Bao, L., Deng, W., Huang, B., Gao, H., Liu, J., Ren, L., Wei, Q., Yu, P., Xu, Y., Qi, F., et al. (2020). The pathogenicity of SARS-CoV-2 in hACE2 transgenic mice. Nature 583, 830–833.

Bardy, C., van den Hurk, M., Eames, T., Marchand, C., Hernandez, R.V., Kellogg, M., Gorris, M., Galet, B., Palomares, V., Brown, J., et al. (2015). Neuronal medium that supports basic synaptic functions and activity of human neurons in vitro. Proc. Natl. Acad. Sci. USA 112, E2725–E2734.

Beers, J., Linask, K.L., Chen, J.A., Siniscalchi, L.I., Lin, Y., Zheng, W., Rao, M., and Chen, G. (2015). A cost-effective and efficient reprogramming platform for large-scale production of integration-free human induced pluripotent stem cells in chemically defined culture. Sci. Rep. 5, 11319.

Bolger, A.M., Lohse, M., and Usadel, B. (2014). Trimmomatic: a flexible trimmer for Illumina sequence data. Bioinformatics 30, 2114–2120.

Bouhaddou, M., Memon, D., Meyer, B., White, K.M., Rezelj, V.V., Correa Marrero, M., Polacco, B.J., Melnyk, J.E., Ulferts, S., Kaake, R.M., et al. (2020). The global phosphorylation landscape of SARS-CoV-2 infection. Cell 182, 685–712.

Brown, P.D., Davies, S.L., Speake, T., and Millar, I.D. (2004). Molecular mechanisms of cerebrospinal fluid production. Neuroscience 129, 957–970.

Cantuti-Castelvetri, L., Ojha, R., Pedro, L.D., Djannatian, M., Franz, J., Kuivanen, S., Kallio, K., Kaya, T., Anastasina, M., Smura, T., et al. (2020). Neuropilin-1 facilitates SARS-CoV-2 cell entry and provides a possible pathway into the central nervous system. bioRxiv. https://doi.org/10.1101/2020.06.07.137802.

Chen, H., and Boutros, P.C. (2011). VennDiagram: a package for the generation of highly-customizable Venn and Euler diagrams in R. BMC Bioinformatics 12, 35.

Chen, R., Wang, K., Yu, J., Howard, D., French, L., Chen, Z., Wen, C., and Xu, Z. (2020). The spatial and cell-type distribution of SARS-CoV-2 receptor ACE2 in human and mouse brain. bioRxiv. https://doi.org/10.1101/2020.04.07.030650.

Chiang, C.H., Su, Y., Wen, Z., Yoritomo, N., Ross, C.A., Margolis, R.L., Song, H., and Ming, G.L. (2011). Integration-free induced pluripotent stem cells derived from schizophrenia patients with a Dros. Inf. Serv.C1 mutation. Mol. Psychiatry 16, 358–360.

Clevers, H. (2016). Modeling development and disease with organoids. Cell 165, 1586–1597.

Desforges, M., Le Coupanec, A., Stodola, J.K., Meessen-Pinard, M., and Talbot, P.J. (2014). Human coronaviruses: viral and cellular factors involved in neuroinvasiveness and neuropathogenesis. Virus Res. 194, 145–158.

Dobin, A., Davis, C.A., Schlesinger, F., Drenkow, J., Zaleski, C., Jha, S., Batut, P., Chaisson, M., and Gingeras, T.R. (2013). STAR: ultrafast universal RNA-seq aligner. Bioinformatics 29, 15–21.

Dong, L., Tian, J., He, S., Zhu, C., Wang, J., Liu, C., and Yang, J. (2020). Possible vertical transmission of SARS-CoV-2 from an infected mother to her newborn. JAMA 323, 1846–1848.

Dubé, M., Le Coupanec, A., Wong, A.H.M., Rini, J.M., Desforges, M., and Talbot, P.J. (2018). Axonal transport enables neuron-to-neuron propagation of human coronavirus OC43. J. Virol. 92, e00404-18.

Ellul, M.A., Benjamin, L., Singh, B., Lant, S., Michael, B.D., Easton, A., Kneen, R., Defres, S., Sejvar, J., and Solomon, T. (2020). Neurological associations of COVID-19. Lancet Neurol. 19, 767–783.

Cell Stem Cell
Short Article

CellPress

Engelhardt, B., and Tietz, S. (2015). Brain barriers: crosstalk between complex tight junctions and adherens junctions. J. Cell Biol. *209*, 493–506.

Farhadian, S., Glick, L.R., Vogels, C.B.F., Thomas, J., Chiarella, J., Casanovas-Massana, A., Zhou, J., Odio, C., Vijayakumar, P., Geng, B., et al. (2020). Acute encephalopathy with elevated CSF inflammatory markers as the initial presentation of COVID-19. BMC Neurol. *20*, 248.

Ghersi-Egea, J.F., Strazielle, N., Catala, M., Silva-Vargas, V., Doetsch, F., and Engelhardt, B. (2018). Molecular anatomy and functions of the choroidal blood-cerebrospinal fluid barrier in health and disease. Acta Neuropathol. *135*, 337–361.

Giorgianni, A., Vinacci, G., Agosti, E., Cariddi, L.P., Mauri, M., Baruzzi, F., and Versino, M. (2020). Transient acute-onset tetraparesis in a COVID-19 patient. Spinal Cord *58*, 1042–1044.

Harcourt, J., Tamin, A., Lu, X., Kamili, S., Sakthivel, S.K., Murray, J., Queen, K., Tao, Y., Paden, C.R., Zhang, J., et al. (2020). Severe acute respiratory syndrome coronavirus 2 from patient with coronavirus disease, United States. Emerg. Infect. Dis. *26*, 1266–1273.

Helms, J., Kremer, S., Merdji, H., Clere-Jehl, R., Schenck, M., Kummerlen, C., Collange, O., Boulay, C., Fafi-Kremer, S., Ohana, M., et al. (2020). Neurologic features in severe SARS-CoV-2 infection. N. Engl. J. Med. *382*, 2268–2270.

Hladky, S.B., and Barrand, M.A. (2016). Fluid and ion transfer across the blood-brain and blood-cerebrospinal fluid barriers; a comparative account of mechanisms and roles. Fluids Barriers CNS *13*, 19.

Hoffmann, M., Kleine-Weber, H., and Pöhlmann, S. (2020a). A multibasic cleavage site in the spike protein of SARS-CoV-2 is essential for infection of human lung cells. Mol. Cell *78*, 779–784.e5.

Hoffmann, M., Kleine-Weber, H., Schroeder, S., Krüger, N., Herrler, T., Erichsen, S., Schiergens, T.S., Herrler, G., Wu, N.-H., Nitsche, A., et al. (2020b). SARS-CoV-2 cell entry depends on ACE2 and TMPRSS2 and is blocked by a clinically proven protease inhibitor. Cell *181*, 271–280.e8.

Huang, J.T., Leweke, F.M., Oxley, D., Wang, L., Harris, N., Koethe, D., Gerth, C.W., Nolden, B.M., Gross, S., Schreiber, D., et al. (2006). Disease biomarkers in cerebrospinal fluid of patients with first-onset psychosis. PLoS Med. *3*, e428.

Hung, E.C., Chim, S.S., Chan, P.K., Tong, Y.K., Ng, E.K., Chiu, R.W., Leung, C.B., Sung, J.J., Tam, J.S., and Lo, Y.M. (2003). Detection of SARS coronavirus RNA in the cerebrospinal fluid of a patient with severe acute respiratory syndrome. Clin. Chem. *49*, 2108–2109.

Iadecola, C., Anrather, J., and Kamel, H. (2020). Effects of COVID-19 on the nervous system. Cell. Published online August 19, 2020. https://doi.org/10.1016/j.cell.2020.08.028.

Lamers, M.M., Beumer, J., van der Vaart, J., Knoops, K., Puschhof, J., Breugem, T.I., Ravelli, R.B.G., Paul van Schayck, J., Mykytyn, A.Z., Duimel, H.Q., et al. (2020). SARS-CoV-2 productively infects human gut enterocytes. Science *369*, 50–54.

Lau, K.K., Yu, W.C., Chu, C.M., Lau, S.T., Sheng, B., and Yuen, K.Y. (2004). Possible central nervous system infection by SARS coronavirus. Emerg. Infect. Dis. *10*, 342–344.

Lawrence, M., Huber, W., Pages, H., Aboyoun, P., Carlson, M., Gentleman, R., Morgan, M.T., and Carey, V.J. (2013). Software for computing and annotating genomic ranges. PLoS Comput. Biol. *9*, e1003118.

Love, M.I., Huber, W., and Anders, S. (2014). Moderated estimation of fold change and dispersion for RNA-seq data with DESeq2. Genome Biol. *15*, 550.

Lun, M.P., Monuki, E.S., and Lehtinen, M.K. (2015). Development and functions of the choroid plexus-cerebrospinal fluid system. Nat. Rev. Neurosci. *16*, 445–457.

Ma-Lauer, Y., Carbajo-Lozoya, J., Hein, M.Y., Muller, M.A., Deng, W., Lei, J., Meyer, B., Kusov, Y., von Brunn, B., Bairad, D.R., et al. (2016). p53 down-regulates SARS coronavirus replication and is targeted by the SARS-unique domain and PLpro via E3 ubiquitin ligase RCHY1. Proc. Natl. Acad. Sci. USA *113*, E5192–E5201.

Mao, L., Jin, H., Wang, M., Hu, Y., Chen, S., He, Q., Chang, J., Hong, C., Zhou, Y., Wang, D., et al. (2020). Neurologic manifestations of hospitalized patients with coronavirus disease 2019 in Wuhan, China. JAMA Neurol. *77*, 683–690.

Matsuyama, S., Nao, N., Shirato, K., Kawase, M., Saito, S., Takayama, I., Nagata, N., Sekizuka, T., Katoh, H., Kato, F., et al. (2020). Enhanced isolation of SARS-CoV-2 by TMPRSS2-expressing cells. Proc. Natl. Acad. Sci. USA *117*, 7001–7003.

McCarthy, D.J., Campbell, K.R., Lun, A.T., and Wills, Q.F. (2017). Scater: pre-processing, quality control, normalization and visualization of single-cell RNA-seq data in R. Bioinformatics *33*, 1179–1186.

Mi, H., Muruganujan, A., Ebert, D., Huang, X., and Thomas, P.D. (2019). PANTHER version 14: more genomes, a new PANTHER GO-slim and improvements in enrichment analysis tools. Nucleic Acids Res. *47*, D419–D426.

Ming, G.L., Tang, H., and Song, H. (2016). Advances in Zika virus research: stem cell models, challenges, and opportunities. Cell Stem Cell *19*, 690–702.

Monteil, V., Kwon, H., Prado, P., Hagelkrüys, A., Wimmer, R.A., Stahl, M., Leopoldi, A., Garreta, E., Hurtado Del Pozo, C., Prosper, F., et al. (2020). Inhibition of SARS-CoV-2 infections in engineered human tissues using clinical-grade soluble human ACE2. Cell *181*, 905–913.e7.

Moriguchi, T., Harii, N., Goto, J., Harada, D., Sugawara, H., Takamino, J., Ueno, M., Sakata, H., Kondo, K., Myose, N., et al. (2020). A first case of meningitis/encephalitis associated with SARS-coronavirus-2. Int. J. Infect. Dis. *94*, 55–58.

Murphy, O.C., Merwick, A., O'Mahony, O., Ryan, A.M., and McNamara, B. (2018). Familial hemiplegic migraine with asymmetric encephalopathy secondary to ATP1A2 mutation: a case series. J. Clin. Neurophysiol. *35*, e3–e7.

Netland, J., Meyerholz, D.K., Moore, S., Cassell, M., and Perlman, S. (2008). Severe acute respiratory syndrome coronavirus infection causes neuronal death in the absence of encephalitis in mice transgenic for human ACE2. J. Virol. *82*, 7264–7275.

Ou, X., Liu, Y., Lei, X., Li, P., Mi, D., Ren, L., Guo, L., Guo, R., Chen, T., Hu, J., et al. (2020). Characterization of spike glycoprotein of SARS-CoV-2 on virus entry and its immune cross-reactivity with SARS-CoV. Nat. Commun. *11*, 1620.

Pellegrini, L., Bonfio, C., Chadwick, J., Begum, F., Skehel, M., and Lancaster, M.A. (2020). Human CNS barrier-forming organoids with cerebrospinal fluid production. Science *369*, eaaz5626.

Puelles, V.G., Lutgehetmann, M., Lindenmeyer, M.T., Sperhake, J.P., Wong, M.N., Allweiss, L., Chilla, S., Heinemann, A., Wanner, N., Liu, S., et al. (2020). Multiorgan and renal tropism of SARS-CoV-2. N. Engl. J. Med. *383*, 590–592.

Qian, X., Nguyen, H.N., Song, M.M., Hadiono, C., Ogden, S.C., Hammack, C., Yao, B., Hamersky, G.R., Jacob, F., Zhong, C., et al. (2016). Brain-region-specific organoids using mini-bioreactors for modeling ZIKV exposure. Cell *165*, 1238–1254.

Qian, X., Jacob, F., Song, M.M., Nguyen, H.N., Song, H., and Ming, G.L. (2018). Generation of human brain region-specific organoids using a miniaturized spinning bioreactor. Nat. Protoc. *13*, 565–580.

Ramani, A., Müller, L., Niklas Ostermann, P., Gabriel, E., Abida-Islam, P., Müller-Schiffmann, A., Mariappan, A., Goureau, O., Gruell, H., Walker, A., et al. (2020). SARS-CoV-2 targets neurons of 3D human brain organoids. EMBO J. Published online September 2, 2020. https://doi.org/10.15252/embj.2020106230.

Renu, K., Prasanna, P.L., and Valsala Gopalakrishnan, A. (2020). Coronaviruses pathogenesis, comorbidities and multi-organ damage - A review. Life Sci. *255*, 117839.

Rodriguez-Lorenzo, S., Ferreira Francisco, D.M., Vos, R., van Het Hof, B., Rijnsburger, M., Schroten, H., Ishikawa, H., Beaino, W., Bruggmann, R., Kooij, G., et al. (2020). Altered secretory and neuroprotective function of the choroid plexus in progressive multiple sclerosis. Acta Neuropathol. Commun. *8*, 35.

Sachs, N.A., Sawa, A., Holmes, S.E., Ross, C.A., DeLisi, L.E., and Margolis, R.L. (2005). A frameshift mutation in Disrupted in Schizophrenia 1 in an American family with schizophrenia and schizoaffective disorder. Mol. Psychiatry *10*, 758–764.

Sakaguchi, H., Kadoshima, T., Soen, M., Narii, N., Ishida, Y., Ohgushi, M., Takahashi, J., Eiraku, M., and Sasai, Y. (2015). Generation of functional

hippocampal neurons from self-organizing human embryonic stem cell-derived dorsomedial telencephalic tissue. Nat. Commun. *6*, 8896.

Samuels, M.H. (2014). Psychiatric and cognitive manifestations of hypothyroidism. Curr. Opin. Endocrinol. Diabetes Obes. *21*, 377–383.

Schwerk, C., Tenenbaum, T., Kim, K.S., and Schroten, H. (2015). The choroid plexus-a multi-role player during infectious diseases of the CNS. Front. Cell. Neurosci. *9*, 80.

Shang, J., Wan, Y., Luo, C., Ye, G., Geng, Q., Auerbach, A., and Li, F. (2020). Cell entry mechanisms of SARS-CoV-2. Proc. Natl. Acad. Sci. USA *117*, 11727–11734.

Shechter, R., London, A., and Schwartz, M. (2013). Orchestrated leukocyte recruitment to immune-privileged sites: absolute barriers versus educational gates. Nat. Rev. Immunol. *13*, 206–218.

Solomon, I.H., Normandin, E., Bhattacharyya, S., Mukerji, S.S., Keller, K., Ali, A.S., Adams, G., Hornick, J.L., Padera, R.F., Jr., and Sabeti, P. (2020). Neuropathological features of Covid-19. N. Engl. J. Med. *383*, 989–992.

Sullivan, G.M., Hatterer, J.A., Herbert, J., Chen, X., Roose, S.P., Attia, E., Mann, J.J., Marangell, L.B., Goetz, R.R., and Gorman, J.M. (1999). Low levels of transthyretin in the CSF of depressed patients. Am. J. Psychiatry *156*, 710–715.

Sun, S.-H., Chen, Q., Gu, H.-J., Yang, G., Wang, Y.-X., Huang, X.-Y., Liu, S.-S., Zhang, N.-N., Li, X.-F., Xiong, R., et al. (2020). A mouse model of SARS-CoV-2 infection and pathogenesis. Cell Host Microbe *28*, 124–133.e4.

Tang, H., Hammack, C., Ogden, S.C., Wen, Z., Qian, X., Li, Y., Yao, B., Shin, J., Zhang, F., Lee, E.M., et al. (2016). Zika virus infects human cortical neural progenitors and attenuates their growth. Cell Stem Cell *18*, 587–590.

Tay, M.Z., Poh, C.M., Renia, L., MacAry, P.A., and Ng, L.F.P. (2020). The trinity of COVID-19: immunity, inflammation and intervention. Nat. Rev. Immunol. *20*, 363–374.

The Gene Ontology Consortium (2019). The Gene Ontology Resource: 20 years and still GOing strong. Nucleic Acids Res. *47*, D330–D338.

Valiuddin, H., Skwirsk, B., and Paz-Arabo, P. (2020). Acute transverse myelitis associated with SARS-CoV-2: a case-report. Brain Behav. Immun. Health *5*, 100091.

Varatharaj, A., Thomas, N., Ellul, M.A., Davies, N.W.S., Pollak, T.A., Tenorio, E.L., Sultan, M., Easton, A., Breen, G., Zandi, M., et al. (2020). Neurological and neuropsychiatric complications of COVID-19 in 153 patients: a UK-wide surveillance study. Lancet Psychiatry *7*, 875–882.

Virani, A., Rabold, E., Hanson, T., Haag, A., Elrufay, R., Cheema, T., Balaan, M., and Bhanot, N. (2020). Guillain-Barré syndrome associated with SARS-CoV-2 infection. IDCases *20*, e00771.

Vivanti, A.J., Vauloup-Fellous, C., Prevot, S., Zupan, V., Suffee, C., Do Cao, J., Benachi, A., and De Luca, D. (2020). Transplacental transmission of SARS-CoV-2 infection. Nat. Commun. *11*, 3572.

Vu, M., Li, R., Baskfield, A., Lu, B., Farkhondeh, A., Gorshkov, K., Motabar, O., Beers, J., Chen, G., Zou, J., et al. (2018). Neural stem cells for disease modeling and evaluation of therapeutics for Tay-Sachs disease. Orphanet J. Rare Dis. *13*, 152.

Wang, M., Cao, R., Zhang, L., Yang, X., Liu, J., Xu, M., Shi, Z., Hu, Z., Zhong, W., and Xiao, G. (2020). Remdesivir and chloroquine effectively inhibit the recently emerged novel coronavirus (2019-nCoV) in vitro. Cell Res. *30*, 269–271.

Watanabe, M., Kang, Y.J., Davies, L.M., Meghpara, S., Lau, K., Chung, C.Y., Kathiriya, J., Hadjantonakis, A.K., and Monuki, E.S. (2012). BMP4 sufficiency to induce choroid plexus epithelial fate from embryonic stem cell-derived neuroepithelial progenitors. J. Neurosci. *32*, 15934–15945.

Wen, Z., Nguyen, H.N., Guo, Z., Lalli, M.A., Wang, X., Su, Y., Kim, N.S., Yoon, K.J., Shin, J., Zhang, C., et al. (2014). Synaptic dysregulation in a human iPS cell model of mental disorders. Nature *515*, 414–418.

Weng, Y.-L., An, R., Cassin, J., Joseph, J., Mi, R., Wang, C., Zhong, C., Jin, S.-G., Pfeifer, G.P., Bellacosa, A., et al. (2017). An intrinsic epigenetic barrier for functional axon regeneration. Neuron *94*, 337–346.e6.

WHO (2020). Coronavirus disease (COVID-19) situation dashboard. https://covid19.who.int/.

Xia, S., Liu, M., Wang, C., Xu, W., Lan, Q., Feng, S., Qi, F., Bao, L., Du, L., Liu, S., et al. (2020). Inhibition of SARS-CoV-2 (previously 2019-nCoV) infection by a highly potent pan-coronavirus fusion inhibitor targeting its spike protein that harbors a high capacity to mediate membrane fusion. Cell Res. *30*, 343–355.

Xu, J., Zhong, S., Liu, J., Li, L., Li, Y., Wu, X., Li, Z., Deng, P., Zhang, J., Zhong, N., et al. (2005). Detection of severe acute respiratory syndrome coronavirus in the brain: potential role of the chemokine mig in pathogenesis. Clin. Infect. Dis. *41*, 1089–1096.

Xu, M., Lee, E.M., Wen, Z., Cheng, Y., Huang, W.K., Qian, X., Tcw, J., Kouznetsova, J., Ogden, S.C., Hammack, C., et al. (2016). Identification of small-molecule inhibitors of Zika virus infection and induced neural cell death via a drug repurposing screen. Nat. Med. *22*, 1101–1107.

Yang, L., Han, Y., Nilsson-Payant, B.E., Gupta, V., Wang, P., Duan, X., Tang, X., Zhu, J., Zhao, Z., Jaffré, F., et al. (2020a). A human pluripotent stem cell-based platform to study SARS-CoV-2 tropism and model virus infection in human cells and organoids. Cell Stem Cell *27*, 125–136.e7.

Yang, X., Yu, Y., Xu, J., Shu, H., Xia, J., Liu, H., Wu, Y., Zhang, L., Yu, Z., Fang, M., et al. (2020b). Clinical course and outcomes of critically ill patients with SARS-CoV-2 pneumonia in Wuhan, China: a single-centered, retrospective, observational study. Lancet Respir. Med. *8*, 475–481.

Ye, M., Ren, Y., and Lv, T. (2020). Encephalitis as a clinical manifestation of COVID-19. Brain Behav. Immun. *88*, 945–946.

Yoon, K.J., Nguyen, H.N., Ursini, G., Zhang, F., Kim, N.S., Wen, Z., Makri, G., Nauen, D., Shin, J.H., Park, Y., et al. (2014). Modeling a genetic risk for schizophrenia in iPSCs and mice reveals neural stem cell deficits associated with adherens junctions and polarity. Cell Stem Cell *15*, 79–91.

Zeng, H., Xu, C., Fan, J., Tang, Y., Deng, Q., Zhang, W., and Long, X. (2020). Antibodies in infants born to mothers with COVID-19 pneumonia. JAMA *323*, 1848–1849.

Zhou, J., Li, C., Liu, X., Chiu, M.C., Zhao, X., Wang, D., Wei, Y., Lee, A., Zhang, A.J., Chu, H., et al. (2020). Infection of bat and human intestinal organoids by SARS-CoV-2. Nat. Med. *26*, 1077–1083.

Cell Stem Cell
Short Article

CellPress

STAR★METHODS

KEY RESOURCES TABLE

REAGENT or RESOURCE	SOURCE	IDENTIFIER
Antibodies		
Goat polyclonal anti-Doublecortin (C-18)	Santa Cruz Biotechnology	Cat# sc-8066, RRID: AB_2088494
Goat polyclonal anti-Nestin (C-20)	Santa Cruz Biotechnology	Cat# sc-21247, RRID: AB_650014
Goat polyclonal anti-OTX2	R&D Systems	Cat# AF1979, RRID: AB_2157172
Goat polyclonal anti-SOX2 (Y-17)	Santa Cruz Biotechnology	Cat# sc-17320, RRID: AB_2286684
Guinea Pig polyclonal anti-MAP2	Synaptic Systems	Cat# 188004, RRID: AB_2138181
Guinea Pig polyclonal anti-OTP	Takara Bio	Cat# M195
Mouse monoclonal anti-AQP1	Santa Cruz Biotechnology	Cat# sc-32737, RRID: AB_626693
Mouse monoclonal anti-dsRNA (J2)	Scicons	Cat# 10010200, RRID: AB_2651015
Mouse monoclonal anti-GFAP (GA5)	Millipore	Cat# MAB360, RRID: AB_11212597
Mouse monoclonal anti-phospho-p38	Santa Cruz	Cat# sc-7973, RRID: AB_670359
Mouse monoclonal anti-PROX1	Millipore	Cat# MAB5654, RRID: AB_2170714
Mouse monoclonal anti-SARS-CoV-2 Nucleoprotein	Sino Biological	Cat# 40143-R001, RRID: AB_2827974
Mouse monoclonal anti-TH	ImmunoStar	Cat# 22941, RRID: AB_572268
Rabbit polyclonal anti-ACE2	Abcam	Cat# ab15348, RRID: AB_301861
Rabbit polyclonal anti-FOXG1	Abcam	Cat# ab18259, RRID: AB_732415
Rabbit polyclonal anti-GFAP	Agilent Dako	Cat# Z033429-2, RRID: AB_10013382
Rabbit polyclonal anti-LMX1A	Novus biological	Cat# NBP2-41193
Rabbit polyclonal anti-PU.1	Cell Signaling Technology	Cat# 2266, RRID: AB_10692379
Rabbit polyclonal anti-TTR	Agilent	Cat# A000202, RRID: AB_578466
Rat polyclonal anti-CTIP2	Abcam	Cat# ab18465, RRID: AB_2064130
Donkey anti-Goat IgG (H+L) Highly Cross-Adsorbed Secondary Antibody, Alexa Fluor 488	Thermo Fisher Scientific	Cat# A-11055, RRID: AB_2534102
Donkey polyclonal anti-Goat IgG (H+L) Cross-Adsorbed Secondary Antibody, Alexa Fluor 647	Thermo Fisher Scientific	Cat# A-21447, RRID: AB_2535864
Donkey polyclonal anti-Guinea Pig IgG (H+L) AffiniPure Secondary Antibody, Alexa Fluor 488	Jackson ImmunoResearch	Cat# 706-545-148, RRID: AB_2340472
Donkey polyclonal anti-Guinea Pig IgG (H+L) AffiniPure Secondary Antibody, Alexa Fluor 647	Jackson ImmunoResearch	Cat# 706-605-148, RRID: AB_2340476
Donkey polyclonal anti-Mouse IgG (H+L) Highly Cross-Adsorbed Secondary Antibody, Alexa Fluor 488	Thermo Fisher Scientific	Cat# A-21202, RRID: AB_141607
Donkey polyclonal anti-Mouse IgG (H+L) Highly Cross-Adsorbed Secondary Antibody, Alexa Fluor 555	Thermo Fisher Scientific	Cat# A-31570, RRID: AB_2536180
Donkey polyclonal anti-Mouse IgG (H+L) Highly Cross-Adsorbed Secondary Antibody, Alexa Fluor 568	Thermo Fisher Scientific	Cat# A-10037, RRID: AB_2534013
Donkey polyclonal anti-Rabbit IgG (H+L) Highly Cross-Adsorbed Secondary Antibody, Alexa Fluor 488	Thermo Fisher Scientific	Cat# A-21206, RRID: AB_2535792

(Continued on next page)

Continued

REAGENT or RESOURCE	SOURCE	IDENTIFIER
Donkey polyclonal anti-Rabbit IgG (H+L) Highly Cross-Adsorbed Secondary Antibody, Alexa Fluor 555	Thermo Fisher Scientific	Cat# A-31572, RRID: AB_162543
Donkey anti-Rabbit IgG (H+L) Highly Cross-Adsorbed Secondary Antibody, Alexa Fluor 568	Thermo Fisher Scientific	Cat# A-10042, RRID: AB_2534017
Donkey anti-Rabbit IgG (H+L) Highly Cross-Adsorbed Secondary Antibody, Alexa Fluor 647	Thermo Fisher Scientific	Cat# A-31573, RRID: AB_2536183
Donkey anti-Rat IgG (H+L) Highly Cross-Adsorbed Secondary Antibody, Alexa Fluor 488	Thermo Fisher Scientific	Cat# A-21208, RRID: AB_2535794
Goat polyclonal anti-Human IgG (H+L) Highly Cross-Adsorbed Secondary Antibody, Alexa Fluor 568	Thermo Fisher Scientific	Cat# A-21090, RRID: AB_2535746
Biological Samples		
Human SARS-CoV-2 convalescent serum	De-identified COVID-19 patient from UCSD Hillcrest Hospital	N/A
Human primary astrocytes	ScienCell Research Laboratories	1800
Human primary choroid plexus epithelial cells	ScienCell Research Laboratories	1310
Chemicals, Peptides, and Recombinant Proteins		
2-Mercaptoethanol	Thermo Fisher Scientific	21985023
Anti-adherence Rinsing Solution	StemCell Technologies, Inc.	07010
Ascorbic acid	Sigma-Aldrich	A0278
B-27 Supplement (50X), minus vitamin A	Thermo Fisher Scientific	12587010
Bovine serum albumin (BSA)	Sigma-Aldrich	Cat# B6917; CAS# 9048-46-8
BrainPhys medium	StemCell Technologies, Inc.	05790
CHIR-99021	StemCell Technologies, Inc.	72054
DAPI	Sigma-Aldrich	Cat# 10236276001; CAS# 28718-90-3
Dibutyryl cyclic AMP	Sigma-Aldrich	D0627
Dimethyl sulfoxide (DMSO)	Sigma-Aldrich	Cat# D2650; CAS# 67-68-5
Dulbecco's Modified Eagle Medium/Nutrient Mixture F-12 (DMEM/F-12)	Thermo Fisher Scientific	11320033
Dulbecco's phosphate-buffered saline (DPBS), calcium, magnesium	Thermo Fisher Scientific	14040133
Dulbecco's phosphate-buffered saline (DPBS), no calcium, no magnesium	Thermo Fisher Scientific	14190144
Fast SYBR Green Master Mix	Thermo Fisher Scientific	4385612
Formaldehyde, 16%, methanol free, Ultra Pure	Polysciences	Cat# 18814-10; CAS#: 50-00-0
GlutaMAX supplement	GIBCO	35050061
Human insulin solution	Sigma-Aldrich	Cat# I9278; CAS# 11061-68-0
IWP-2	StemCell Technologies, Inc.	72122
KnockOut Serum Replacement	Thermo Fisher Scientific	10828028
Laminin from Engelbreth-Holm-Swarm murine sarcoma basement membrane	Sigma-Aldrich	L2020
LDN-193189	StemCell Technologies, Inc.	72147
Matrigel (hESC-qualified)	Corning	08774552
MEM Non-Essential Amino Acids Solution (100X)	Thermo Fisher Scientific	11140050

Cell Stem Cell
Short Article

CellPress

Continued

REAGENT or RESOURCE	SOURCE	IDENTIFIER
mTeSR Plus	StemCell Technologies, Inc.	05825
N-2 Supplement (100X)	Thermo Fisher Scientific	17502048
Neurobasal medium	Thermo Fisher Scientific	21103049
5% normal donkey serum	Jackson ImmunoResearch	017-000-121
Nuclease-Free Water (not DEPC-Treated)	Thermo Fisher Scientific	AM9937
Penicillin-Streptomycin (5,000 U/mL)	Thermo Fisher Scientific	15070063
Poly-L-ornithine	Sigma-Aldrich	P4957
Purmorphamine	Tocris	455110
Recombinant Human BMP-7	Peprotech	120-03P
Recombinant Human/Murine/Rat BDNF	Peprotech	450-02
Recombinant Human GDNF	Peprotech	450-10
Recombinant Human SHH	BioLegend	753506
SB-431542	StemCell Technologies, Inc.	72234
SuperScript III First-Strand Synthesis System	Thermo Fisher Scientific	18080051
Tissue Freezing Medium	General Data	1518313
Triton X-100	Sigma-Aldrich	Cat# T9284; CAS# 9002-93-1
TRIzol reagent	Thermo Fisher Scientific	15596026
TrueBlack Lipofuscin Autofluorescence Quencher	Biotium	23007
TWEEN 20	Sigma-Aldrich	Cat# P1379; CAS# 9005-64-5
VECTASHIELD Vibrance Antifade Mounting Medium	Vector Laboratories	H170010
Y-27632	StemCell Technologies, Inc.	Cat# 72304; CAS# 129830-38-2
Critical Commercial Assays		
Click-iT TUNEL Alexa Fluor 647 Imaging Assay	Thermo Fisher Scientific	C10247
EZ-PCR Mycoplasma test kit	Biological Industries	2070020
NextSeq High Output v2 150 Cycles	Illumina	TG-160-2002
Qubit dsDNA HS Assay Kit	Thermo Fisher Scientific	Q33231
Deposited Data		
CPO Bulk RNA sequencing	This paper	GEO: GSE157852
Experimental Models: Cell Lines		
Human C1-2 iPSC line	Wen et al., 2014	https://doi.org/10.1038/nature13716
Human C3-1 iPSC line	Wen et al., 2014	https://doi.org/10.1038/nature13716
Human WTC11 iPSC line	Coriell	GM25256
Human HT268A iPSC line	Vu et. al, 2018	https://doi.org/10.1186/s13023-018-0886-3
Human PCS201012 iPSC line	Beers et. al, 2015	https://doi.org/10.1038/srep11319
Human iPSC-derived cortical glutamatergic neurons	BrainXell, Inc.	BX-0300
Human iPSC-derived cortical GABAergic neurons	BrainXell, Inc.	BX-0400
Human iPSC-derived cortical astrocytes	BrainXell, Inc.	BX-0600
Human iPSC-derived microglia	BrainXell, Inc.	BX-0900
Vero E6 cells	ATCC	CRL-1586
Experimental Models: Organisms/Strains		
SARS-CoV-2 USA-WA1/2020 virus	BEI Resources	NR-52281

(Continued on next page)

Continued

REAGENT or RESOURCE	SOURCE	IDENTIFIER
Oligonucleotides		
QPCR Primers (Refer to Table S1 for sequences)	IDT	Custom
Software and Algorithms		
Adobe Illustrator CC	Adobe	https://www.adobe.com/products/illustrator.html; RRID: SCR_010279
Adobe Photoshop CC	Adobe	https://www.adobe.com/products/photoshop.html; RRID: SCR_014199
bcl2fastq v2.17.1.14	Illumina	https://support.illumina.com/sequencing/sequencing_software/bcl2fastq-conversion-software.html; RRID: SCR_015058
Columbus Image Data Storage and Analysis System	Perkin Elmer	https://www.perkinelmer.com/Product/image-data-storage-and-analysis-system-columbus
DESeq2 v1.24.0	Love et al., 2014	https://bioconductor.org/packages/release/bioc/html/DESeq2.html; RRID: SCR_015687
EnhancedVolcano v1.7.8	GitHub	https://github.com/kevinblighe/EnhancedVolcano
GenomicFeatures v1.36.4	Lawrence et al., 2013	http://bioconductor.org/packages/release/bioc/html/GenomicFeatures.html; RRID: SCR_016960
GraphPad Prism	GraphPad Software	https://www.graphpad.com/scientific-software/prism/; RRID: SCR_002798
Human genome release 28 (GRCh38.p12)	GENCODE	https://www.gencodegenes.org/human/release_28.html
ImageJ	NIH	https://imagej.nih.gov/ij/; RRID: SCR_003070
Imaris	Bitplane	https://imaris.oxinst.com/packages; RRID: SCR_007370
PANTHER v15.0	Mi et al., 2019	http://www.pantherdb.org/; RRID: SCR_004869
R Project v3.6.0	Open source	https://www.r-project.org/; RRID: SCR_001905
RStudio v1.2.1335	Open source	https://rstudio.com/; RRID: SCR_000432
SARS-CoV-2 genome (Wuhan-Hu-1 isolate)	Ensembl	https://covid-19.ensembl.org
scater v1.12.2	McCarthy et al., 2017	https://bioconductor.org/packages/release/bioc/html/scater.html; RRID: SCR_015954
STAR v2.5.2a	Dobin et al., 2013	https://github.com/alexdobin/STAR; RRID: SCR_015899
Trimmomatic v0.32	Bolger et al., 2014	http://www.usadellab.org/cms/index.php?page=trimmomatic; RRID: SCR_011848
VennDiagram v1.6.20	Chen and Boutros, 2011	https://cran.r-project.org/web/packages/VennDiagram/; RRID: SCR_002414
Zen Blue	Carl Zeiss	https://www.zeiss.com/microscopy/us/products/microscope-software/zen-lite.html; RRID: SCR_013672
Other		
6-well ultra-low attachment culture plate	Fisher Scientific	07200601
96-well imaging plate	Greiner Bio-one	655090
Aggrewell 800	StemCell Technologies, Inc.	34821
Bioanalyzer 2100	Agilent	G2939BA

(Continued on next page)

Cell Stem Cell
Short Article

CellPress

Continued

REAGENT or RESOURCE	SOURCE	IDENTIFIER
Cell counting slides	Thermo Fisher Scientific	C10228
Cellometer Mini Cell Counter	Nexcelom	Mini Cell Counter
Cellometer Disposable Counting Chambers	Nexcelom	PD100
Charged microscope slides	Fisher Scientific	22-035813
Countess II Automated Cell Counter	Thermo Fisher Scientific	AMQAX1000
Forma Steri-Cult CO_2 Incubator	Thermo Fisher Scientific	3310
Hydrophobic barrier PAP pen	Vector Laboratories	H-4000
In-VitroCell ES Direct Heat CO_2 Incubator	Nuaire	NU-5710
MaxQ CO_2 Plus Shaker	Thermo Fisher Scientific	88881102
NanoDrop 2000	Thermo Fisher Scientific	ND-2000
NextSeq550	Illumina	SY-415-1002
Qubit 3 Fluorimeter	Thermo Fisher Scientific	Q33216
StepOnePlus Real-Time PCR	Applied Biosystems	4376592
T100 Thermal Cycler	Bio-rad	1861096EDU

RESOURCE AVAILABILITY

Lead Contact
Further information and requests for resources and reagents should be directed to and will be fulfilled by the Lead Contact, Dr. Guo-li Ming (gming@pennmedicine.upenn.edu).

Materials Availability
This study did not generate new unique reagents.

Data and Code Availability
The accession number for the RNA-seq data reported in this paper is GEO: GSE157852. The data that support the findings of this study are available from the Lead Contact, Dr. Guo-li Ming (gming@pennmedicine.upenn.edu) upon reasonable request.

EXPERIMENTAL MODEL AND SUBJECT DETAILS

Human Induced Pluripotent Stem Cells and Convalescent Serum from a Patient with COVID-19
Human iPSC lines used in the current study were derived from healthy donors and were either obtained from commercial sources or previously generated and fully characterized (Chiang et al., 2011; Wen et al., 2014; Yoon et al., 2014). C1-2 hiPSCs were generated from fibroblasts obtained from ATCC (CRL-2097). C3-1 hiPSCs were generated from fibroblasts obtained from an individual in a previously characterized American family (Sachs et al., 2005). WTC11 hiPSC were obtained from Coriell (GM25256). HT268A hiPSCs were generated from dermal fibroblasts obtained from Coriell (GM05659) (Vu et al., 2018), and PCS201012 hiPSCs were generated from dermal fibroblasts obtained from ATCC (PCS-201-012) (Beers et al., 2015). Generation of hiPSC lines followed institutional IRB and ISCRO guidelines and was approved by Johns Hopkins University School of Medicine. Karyotyping analysis by standard G-banding technique was carried out by the Cytogenetics Core Facility at the Johns Hopkins Hospital or Cell Line Genetics. Results were interpreted by clinical laboratory specialists of the Cytogenetics Core or Cell Line Genetics. All hiPSC lines were confirmed free of Mycoplasma, Acholeplasma, and Spiroplasma with a detection limit of 10 CFU/ml by targeted PCR (Biological Industries).

Convalescent serum used for immunofluorescence staining was obtained from a de-identified patient with COVID-19 at the UCSD Hillcrest Hospital with consent and following all institutional IRB and ISCRO guidelines.

METHOD DETAILS

Monolayer Neural Cell Cultures
hiPSC-derived cortical astrocytes (BrainXell, Inc.) and microglia (BrainXell, Inc.) were cultured according to the supplier's instructions and plated directly out of thaw onto 96 well imaging plates coated with Poly-L-ornithine at 2 μg/cm^2 and laminin from Engelbreth-Holm-Swarm murine sarcoma basement membrane at 5 μg/mL at a density of 15,000 cells per well. hiPSC-derived cortical gluta-matergic neurons, cortical GABAergic neurons, and cortical astrocytes (BrainXell, Inc.) were plated according to the supplier's in-structions, mixed together in a ratio of 10,000 GABAergic neurons:10,000 Glutamatergic neurons:5000 astrocytes directly out of

thaw onto 96 well imaging plates coated with Poly-L-ornithine (Sigma-Aldrich) at 2 $\mu g/cm^2$ and laminin from Engelbreth-Holm-Swarm murine sarcoma basement membrane (Sigma-Aldrich) at 5 $\mu g/mL$. The day after plating the media was removed, and replaced with BrainPhys medium (StemCell Technologies) with 1% N2 (ThermoFisher Scientific), 2% B27 (ThermoFisher Scientific), 1% Pen-strep (ThermoFisher Scientific), and supplemented with recombinant Brain-derived Neurotrophic Factor (BDNF, 20 ng/ml; Peprotech), recombinant Glia-derived Neurotrophic Factor (GDNF, 20 ng/ml; Peprotech), ascorbic acid (200 nM; Sigma), dibutyryl cyclic AMP (1 mM; Sigma) and laminin (1 $\mu g/mL$; Sigma-Aldrich) (Bardy et al., 2015). Primary human astrocytes (ScienCell Research Laboratories) were cultured and expanded for two passages, according to the supplier's instructions. After the second expansion, astrocytes were cryopreserved at 250,000 cells per vial. Banked astrocytes were thawed directly onto 96 well imaging plates (Greiner Bio-one) coated with Poly-L-ornithine (Sigma-Aldrich) at 2 $\mu g/cm^2$ and laminin from Engelbreth-Holm-Swarm murine sarcoma basement membrane (Sigma-Aldrich) at 5 $\mu g/mL$ at a density of 16,000 cells per well for shorter infection times (48 hours or less) and 8000 cell per well for 120 hour infections. Primary human choroid plexus epithelial cells (ScienCell Research Laboratories) were cultured according to the supplier's instructions. Cells were either passaged once or plated directly out of thaw onto 96-well imaging plates coated with Poly-L-ornithine at 2 $\mu g/cm^2$ at a density of 4000 cells per well.

Human Induced Pluripotent Stem Cell Culture

All studies involving hiPSCs were performed under approved protocols of the University of Pennsylvania and NIH. Refer to the Key Resources Table for the source of each hiPSCs. All hiPSC lines were confirmed to have a normal karyotype and were confirmed free of Mycoplasma, Acholeplasma, and Spiroplasma with a detection limit of 10 CFU/mL by targeted PCR (Biological Industries). For cortical, hippocampal, hypothalamic, and midbrain organoid generation, hiPSCs were cultured on mouse embryonic fibroblast feeder (MEF) cells in stem cell medium consisting of DMEM:F12 supplemented with 20% KnockOut Serum Replacement, 1X MEM-NEAAs, 1X GlutaMAX, 1X Penicillin-Streptomycin, 1X 2-mercaptoethanol, and 10 ng/mL bFGF in a 5% CO_2, 37°C, 90% relative humidity incubator as previously described (Qian et al., 2018). Culture medium was replaced every day. hiPSCs were passaged every week onto a new tissue-treated culture plate coated with 0.1% gelatin for 2 hours and pre-seeded with γ-irradiated CF1 MEF cells one day in advance. Colonies were detached by washing with DPBS and treating with 1 mg/mL Collagenase Type IV for 30-60 minutes. Detached colonies were washed 3 times with 5 mL DMEM:F12 and dissociated into small clusters by trituration with a P1000 pipette. For CPO generation, hiPSCs were maintained in feeder-free conditions on plates pre-coated with hESC-qualified Matrigel (Corning) using mTeSR Plus medium (StemCell Technologies, Inc.). Culture medium was replaced every other day and hiPSCs were passaged every week by washing with DPBS and incubating with ReLeSR reagent (StemCell Technologies, Inc.) for 5 minutes. Detached hiPSCs were broken into smaller clusters by gentle trituration using a 5 mL pipette and seeded onto fresh coated plates.

Brain Organoid Cultures

Generation of cortical organoids from C3-1 hiPSCs was performed as previously described (Qian et al., 2016, 2018). Briefly, hiPSC colonies were detached with Collagenase Type IV, washed with DMEM:F12, and transferred to an ultra-low attachment 6-well plate (Corning Costar) in neural induction medium containing DMEM:F12 supplemented with 20% KnockOut Serum Replacement, 1X MEM-NEAAs, 1X GlutaMax, 1X Penicillin-Streptomycin, 1X 2-mercaptoethanol, 2 μM Dorsomorphin and 2 μM A83-01. On Day 5 and Day 6, half of the medium was replaced with forebrain induction medium consisting of DMEM:F12 supplemented with 1X N2 supplement, 1X Penicillin/Streptomycin, 1X Non-essential Amino Acids, 1X GlutaMax, 1 μM CHIR99021, and 1 μM SB-431542. On Day 7, organoids were embedded in Matrigel and cultured in forebrain induction medium for 7 more days. On Day 14, embedded organoids were mechanically dissociated from Matrigel and transferred to a 6 well-plate on a CO_2 resistant orbital shaker (ThermoFisher) and grown in differentiation medium consisting of DMEM:F12 supplemented with 1X N2 supplement, 1X B27 supplement, 1X Penicillin/Streptomycin, 1X 2-Mercaptoethanol, 1X Non-essential Amino Acids, and 2.5 g/mL human insulin. From Day 35 until the point of sampling, extracellular matrix (ECM) proteins were supplemented in differentiation medium by dissolving Matrigel at 1% (v/v). To generate midbrain organoids from HT268A and PCS201012 hiPSCs, hiPSC colonies were transferred to an Ultra-Low attachment 6-well plate containing Midbrain Induction Medium 1, consisting of DMEM:F12, 20% Knockout Serum Replacer, 1X Glutamax, 1X 2-Mercaptoenthanol, 1x Pen/Strep, 100 nM LDN-193189, 10 μM SB-431542, 2 μM Purmorphamine, 100 ng/mL SHH, 100 ng/mL FGF-8. On day 5, cultures were switched to Midbrain Induction Medium 2, consisting of DMEM:F12, 1X N2 Supplement, 1X Glutamax, 1x Pen/Strep, 100 nM LDN-193189, 3 μM CHIR-99021, 2 μM Purmorphamine, 100 ng/ml SHH, 100 ng/ml FGF-8. On day 7, EBs with smooth and round edges were selected, switched to Midbrain Induction Medium 3, consisting of DMEM:F12, 1X N2 Supplement, 1X Glutamax, 1x Pen/Strep, 100 nM LDN-193189, 3 μM CHIR-99021, and transferred to a shaking platform. On day 14, cultures were switched to Differentiation Medium, consisting of Neurobasal Medium, 1X B27 Supplement, 1X Glutamax, 1X 2-Mercaptoenthanol, 20 ng/mL BDNF, 20 ng/mL GDNF, 0.2 mM Ascorbic Acid, 1 ng/mL TGFβ, and 0.5 mM c-AMP. For generation of hippocampal organoids from C1-2 and WTC11 hiPSC lines, cortical induction medium was replaced with medium containing 3 μM CHIR-99021 and 20 ng/mL recombinant human BMP-7. For generation of hypothalamic organoids from C1-2 and C3-1 hiPSC lines, hiPSC colonies were processed similarly to those for cortical organoids followed by exposure to Shh signaling and Wnt-inhibition in induction medium with 50 ng/mL recombinant Sonic Hedgehog, 1 μM Purmorphamine, 10 μM IWR1-endo and 1 μM SAG, and then transferred to differentiation medium for further culture. Organoids were maintained with media changes every other day.

Cell Stem Cell
Short Article

 CellPress

Choroid Plexus Organoid Culture

At 70% confluence, undifferentiated hiPSCs (C1-2 and WTC11 lines) grown in feeder-free conditions were detached using ReLeSR reagent and gently triturated into small clusters using a 5 mL pipette and pipette aid. hiPSC clusters were centrifuged at 200 g for 3 minutes and the supernatant was aspirated and replaced with mTeSR Plus medium supplemented with 10 μM Y-27632. Approximately 5,000 hiPSCs were aggregated into each EB by following instructions using the Aggrewell 800 plate and cultured overnight in mTeSR Plus medium supplemented with 10 μM Y-27632. The next day (Day 1), embryoid bodies were gently removed from the Aggrewell plate using a P1000 pipettor with a wide-bore tip, washed three times with DMEM:F12, and transferred to neural induction medium containing DMEM:F12 supplemented with 20% KnockOut Serum Replacement, 1X MEM-NEAAs, 1X GlutaMax, 1X Penicillin-Streptomycin, 1X 2-mercaptoethanol, 0.5 μM LDN-193189, 5 μM SB-431542, 1 μM IWP-2, and 10 μM Y-27632 in ultra-low attachment 6-well plates with 4 mL of medium per well. On day 8, EBs were washed with DMEM:F12 and transferred to non-treated 6-well plates with 4 mL choroid plexus induction medium containing DMEM:F12 supplemented with 1X N2 supplement, 1X Penicillin/Streptomycin, 1X Non-essential Amino Acids, 1X GlutaMax, 3 μM CHIR-99021, and 200 ng/mL human recombinant BMP-7 per well. From this point onward, organoids were cultured on an orbital shaker rotating at 110 rpm. No more than 15 EBs were cultured in each well and half of the medium was replaced every 2 days. On day 30, medium was replaced with differentiation medium containing a 1:1 mixture of DMEM/F12 and Neurobasal supplemented with 1X N2 supplement, 1X B27 supplement w/o vitamin A, 1X Penicillin/Streptomycin, 1X Non-essential Amino Acids, 1X GlutaMax, 10 ng/mL BDNF, and 10 ng/mL GDNF. Differentiation medium was replaced every three days and organoids could be maintained for over 100 days.

SARS-CoV-2 Infection of Cultures

SARS-CoV-2 USA-WA1/2020 (Gen Bank: MN985325.1) (Harcourt et al., 2020) viral isolate was obtained from BEI Resources. SARS-CoV-2 virus was expanded and titered using Vero E6 cells. Culture cells were infected in a 96-well plate with 100 μL of medium per well using multiplicity (MOI) of 0.2, 1, or 5, and vehicle-treated cells as controls. After virus exposure for 12 hours, cells were washed 3 times with fresh medium and returned to culture. Brain organoids were infected in a 24-well ultra-low attachment plate (Corning) with 0.5 mL of medium per well containing vehicle, 10^3, 10^4, or 10^5 focus forming units (FFU) of SARS-CoV-2 for 8 hours on an orbital shaker rotating at approximately 100 rpm. After virus exposure, organoids were washed 3 times with fresh medium and returned to culture. For infection of organoids, we controlled the virus titer rather than the MOI since it is not feasible to obtain an accurate cell count on each batch of organoids before infection. According to our estimate, each organoid contains approximately 250-500,000 cells, corresponding to an estimated MOI of 0.1-0.05 when using 10^5 FFU SARS-CoV-2 virus and infecting 4 organoids together.

Tissue Processing and Immunohistology

At experimental endpoints, brain organoids were placed directly in 4% methanol-free formaldehyde (Polysciences) diluted in DPBS (Thermo Fisher Scientific) overnight at 4°C on a rocking shaker. After fixation, brain organoids were washed in DPBS and cryoprotected by overnight incubation in 30% sucrose (Sigma-Aldrich) in DPBS at 4°C. Brain organoids were placed in a plastic cryomold (Electron Microscopy Sciences) and snap frozen in tissue freezing medium (General Data) on dry ice. Frozen tissue was stored at −80°C until processing. Monolayer cells grown on glass coverslips were fixed in 4% methanol-free formaldehyde (Polysciences), diluted in DPBS (ThermoFisher Scientific) for 5 hours at room temperature, washed with DPBS, and stored at 4°C until ready for immunohistology. Serial tissue sections (25 μm for brain organoids) were sliced using a cryostat (Leica, CM3050S), and melted onto charged slides (Thermo Fisher Scientific). Slides were dried at room temperature and stored at −20°C until ready for immunohistology. For immunofluorescence staining, the tissue sections were outlined with a hydrophobic pen (Vector Laboratories) and washed with TBS containing 0.1% Tween-20 (v/v). Tissue sections were permeabilized and non-specific binding was blocked using a solution containing 10% donkey serum (v/v), 0.5% Triton X-100 (v/v), 1% BSA (w/v), 0.1% gelatin (w/v), and 22.52 mg/ml glycine in TBST for 1 hour at room temperature. The tissue sections were incubated with primary antibodies (see the Key Resources Table) diluted in TBST with 5% donkey serum (v/v) and 0.1% Triton X-100 (v/v) overnight at 4°C. After washing in TBST, tissue sections were incubated with secondary antibodies (see the Key Resources Table) diluted in TBST with 5% donkey serum (v/v) and 0.1% Triton X-100 (v/v) for 1.5 hours at room temperature. After washing with TBST, sections were washed with TBS to remove detergent and incubated with True-Black reagent (Biotium) diluted 1:20 in 70% ethanol for 1 minute to block autofluorescence. After washing with TBS, slides were mounted in mounting solution (Vector Laboratories), coverslipped, and sealed with nail polish.

Confocal Microscopy and Image Processing

Monolayer cultures were imaged with a Perkin-Elmer Opera Phenix high-content automatic imaging system with a 20x air objective in confocal mode. At least 9 fields were acquired per well. Images were analyzed using Columbus Image Data Storage and Analysis System. Brain organoid sections were imaged as z stacks using a Zeiss LSM 810 confocal microscope or a Zeiss LSM 710 confocal microscope (Zeiss) using a 10X, 20X, 40X, or 63X objective with Zen 2 software (Zeiss). Images were analyzed using either Imaris 7.6 or ImageJ software. Images were cropped and edited using Adobe Photoshop (Adobe) and Adobe Illustrator (Adobe).

Viral Titer Assay

Tissue culture supernatants and lysates from SARS-CoV-2 treated CPOs were collected at 0, 24, and 72 hpi for 2 biological replicates per time point containing 4 organoids each. Tissue culture supernatants were stored at −80°C until titration. For lysates, organoids

were washed with cold PBS, mechanically dispersed and disrupted by freeze-thaw cycles, and the clarified homogenate was stored at $-80°C$ until titration. Viral titers were determined in Vero E6 cells using an immune focus forming unit assay. Briefly, Vero E6 cells (3×10^4 cells/96-well) were inoculated with 100 μl of serially diluted organoid supernatant or lysate in a 96-well plate at $37°C$ and 5% CO_2 for 20 hours. Cells were fixed with 4% methanol-free paraformaldehyde overnight at $4°C$. Infected foci were labeled using immunofluorescence staining for SARS-CoV-2 nucleoprotein. SARS-CoV-2 nucleoprotein positive cells were counted in each well. Readouts were performed on wells with the highest dilution displaying observable infection.

RNA Isolation, Library Preparation, and Sequencing
To minimize variability due to sampling and processing, each biological replicate consisted of 3 organoids and replicates for all experimental conditions were processed in parallel for RNA-extraction, library preparation and sequencing. At the desired experimental endpoints, organoids were homogenized in TRIzol (Thermo Fisher Scientific) using a disposable pestle and handheld mortar and stored at $-80°C$ until processing. RNA clean-up was performed using the RNA Clean & Concentrator kit (Zymo Research) after TRIzol phase separation according to the manufacturer's protocol. RNA concentration and quality were assessed using a Nanodrop 2000 (Thermo Fisher Scientific).

Library preparation was performed as previously described with some minor modifications (Weng et al., 2017). About 300 ng of RNA in 3.2 μL was combined with 0.25 μL RNase inhibitor (NEB) and 1 μL CDS primer (5′-AAGCAGTGGTATCAACGCAGAG TACT30VN-3′) in an 8-well PCR tube strip, heated to $70°C$ for 2 minutes, and immediately placed on ice. 5.55 μL RT mix, containing 2 μL of 5X SMARTScribe RT buffer (Takara), 0.5 μL of 100 mM DTT (Millipore Sigma), 0.3 μL of 200 mM MgCl2 (Thermo Fisher Scientific), 1 μL of 10 mM dNTPs (Takara), 1 μL of 10 μM TSO primer (5′-AAGCAGTGGTATCAACGCAGAGTACATrGrGrG-3′), 0.25 μL of RNase inhibitor (NEB), and 0.5 μL SMARTScribe reverse transcriptase (Takara) was added to the reaction. RT was performed under the following conditions: $42°C$ for 90 minutes, 10 cycles of $50°C$ for 2 minutes and $42°C$ for 2 minutes, $70°C$ for 15 minutes, and $4°C$ indefinitely. For cDNA amplification, 2 μL of the RT reaction was combined with 2.5 μL of 10X Advantage 2 buffer (Takara), 2.5 μL of 2.5 mM dNTPs (Takara), 0.25 μL of 10 μM IS PCR primer (5′-AAGCAGTGGTATCAACGCAGAGT-3′), 17.25 μL nuclease free water (ThermoFisher), and 0.5 μL Advantage 2 DNA Polymerase (Takara). Thermocycling conditions were as follows: $94°C$ for 3 minutes, 8 cycles of $94°C$ for 15 s, $65°C$ for 30 s, and $68°C$ for 6 minutes, $72°C$ for 10 minutes, and $4°C$ indefinitely. Amplified cDNA was purified using 0.8X AMPure XP beads (Beckman Coulter), eluted in 15 μL nuclease-free water, and quantified using Qubit dsDNA HS assay kit (Thermo Fisher Scientific). cDNA was fragmented by combining 100 pg cDNA in 1 μL nuclease free water, 2X TD buffer (20 mM Tris, pH 8.0; Thermo Fisher Scientific), 10 mM $MgCl_2$, and 16% PEG 8000 (MilliporeSigma), and 0.5 μL Tn5 (Lucigen). The mixture was heated to $55°C$ for 12 minutes, and the reaction was terminated upon the addition of 1.25 μL of 0.2% SDS (Fisher) and incubated at room temperature for 10 minutes. Fragments were amplified by adding 16.75 μL nuclease free water (Thermo Fisher Scientific), 1 μL of 10 mM Nextera i7 primer, 1 μL of 10 mM Nextera i5 primer, and 25 μL KAPA HiFi hotstart readymix (EMSCO/FISHER). Thermocycling conditions were as follows: $72°C$ for 5 minutes, $95°C$ for 1 minute, 14 cycles of $95°C$ for 30 s, $55°C$ for 30 s, and $72°C$ for 30 s, $72°C$ for 1 minute, and $4°C$ indefinitely. DNA was purified twice with 0.8X AMPure XP beads (Beckman Coulter) and eluted in 10 μL of 10 mM Tris, pH 8 (Thermo Fisher Scientific). Samples were quantified by qPCR (KAPA) and pooled at equal molar amounts. Final sequencing library fragment sizes were quantified by bioanalyzer (Agilent) with an average size of $\sim$420 bp, and concentrations were determined by qPCR (KAPA). Samples were loaded at concentrations of 2.7 pM and sequenced on a NextSeq 550 (Illumina) using 1x72 bp reads to an average depth of 40 million reads per sample.

Bioinformatics Analyses
Choroid plexus organoid raw sequencing data were demultiplexed with bcl2fastq2 v2.17.1.14 (Illumina) with adaptor trimming using Trimmomatic v0.32 software (Bolger et al., 2014). Alignment was performed using STAR v2.5.2a (Dobin et al., 2013). A combined reference genome consisting of GENCODE human genome release 28 (GRCh38.p12) and Ensembl SARS-CoV-2 Wuhan-Hu-1 isolate genome (genome assembly: ASM985889v3, GCA_009858895.3; sequence: MN908947.3) was used for alignment. Multimapping and chimeric alignments were discarded, and uniquely mapped reads were quantified at the exon level and summarized to gene counts using STAR -*quantMode GeneCounts*. All further analyses were performed in R v3.6.0. Transcript lengths were retrieved from GTF annotation files using GenomicFeatures v1.36.4 (Lawrence et al., 2013) and raw counts were converted to units of transcripts per million (TPM) using the *calculateTPM* function in scater v1.12.2 (McCarthy et al., 2017). A combined TPM normalization using both human and SARS-CoV-2 viral transcripts was used to obtain TPM values for SARS-CoV-2 viral transcripts. A human-only TPM normalization was used to obtain TPM values for human transcripts.

To compare the transcriptome of CPOs to adult human choroid plexus tissue and hippocampal organoids (HOs), normalization steps were implemented to first make the data comparable. Human choroid plexus raw sequencing data (Rodriguez-Lorenzo et al., 2020) was downloaded from the NCBI Gene Expression Omnibus (GEO: accession number GSE137619). The data was aligned to GRCh38.p12 and raw counts TPM-normalized to parallel CPO and HO datasets. TPM expression values were $\log_{10}(TPM + 1)$ transformed for plotting individual gene expression values. To compare the whole transcriptome of CPOs to adult human choroid plexus tissue and HOs, raw counts were normalized using the variance stabilizing transformation (VST) using DESeq2 v1.24.0 (Love et al., 2014) and correlation analysis was performed by calculating Spearman correlation coefficients in the space of shared genes across the whole transcriptome of all datasets.

Differential gene expression analysis for CPOs between 72 hpi vehicle, 24 hpi SARS-CoV-2 infection, and 72 hpi SARS-CoV-2 infection was performed using DESeq2 v1.24.0 (Love et al., 2014). SARS-CoV-2 viral transcripts were removed for differential

Cell Stem Cell
Short Article

CellPress

gene expression analysis. Variance stabilizing transformation (VST) of raw counts was performed prior to whole-transcriptome principal component analysis (PCA) using DESeq2 v1.24.0. Upregulated and downregulated genes for 24 hpi SARS-CoV-2 compared to 72 hpi vehicle, and 72 hpi SARS-CoV-2 compared to 72 hpi vehicle were filtered by adjusted p value < 0.05. Volcano plots for 24 hpi SARS-CoV-2 and 72 hpi SARS-CoV-2 were plotted using EnhancedVolcano v1.7.8. Shared and unique signatures for upregulated and downregulated genes between 24 hpi SARS-CoV-2 and 72 hpi SARS-CoV-2 were visualized using VennDiagram v1.6.20 (Chen and Boutros, 2011). Upregulated and downregulated gene lists for each time point were used for GO (Ashburner et al., 2000; The Gene Ontology Consortium, 2019) enrichment analysis using PANTHER v15.0 (Mi et al., 2019). For each gene list, a list of terms for GO biological process complete, GO molecular function complete, and GO cellular component complete were filtered by false discovery rate (FDR) < 0.05. Selected genes from notable GO terms were $\log_2(TPM + 1)$ normalized and converted to row Z-scores per gene for visualization.

For SARS-CoV-2 cross-organoid comparison analysis, a list of upregulated and downregulated differentially expressed genes (DEGs) after SARS-CoV-2 infection were downloaded for adult hepatocyte organoids at 24 hpi (Yang et al., 2020a), intestinal organoids at 60 hpi in expansion (EXP) medium (Lamers et al., 2020), and intestinal organoids at 60 hpi in differentiation (DIF) medium (Lamers et al., 2020). Upregulated and downregulated genes were filtered by adjusted p value < 0.05. Shared and unique signatures for upregulated and downregulated genes for the total gene set for CPOs (24 hpi and 72 hpi SARS-CoV-2), adult hepatocyte organoids (24 hpi SARS-CoV-2), and intestinal organoids (60 hpi SARS-CoV-2 in EXP medium and 60 hpi SARS-CoV-2 in DIF medium) were visualized using VennDiagram v1.6.20.

Quantitative PCR Validation

Primer sequences are listed in Figure S1. About 0.5-1.5 μg RNA was used to generate the cDNA for QPCR with SuperScript III First-Strand Synthesis System (Thermo Fisher Scientific) according to manufacturer's protocol. For QPCR reaction, 2 μL of cDNA was mixed with 6 μL of nuclease free water, 1 μL of 10 mM forward primer, 1 μL of 10 mM reverse primer and 10 μL of SYBR Green qPCR Master Mix (Thermo Fisher Scientific), and the QPCR reactions were performed on the StepOnePlus Real-Time PCR System (Applied Biosystems). Thermocycling conditions were as follows: 95°C for 20 s, 44 cycles of 95°C for 3 s and 60°C for 30 s. The difference between the Ct values (ΔCt) of the genes of interest and ACTIN gene was calculated for each experimental sample, and 2^(-ΔΔCt) was used to calculate the fold-change in expression of the genes of interest between samples using 20 DIV HOs as the reference for Figure S2D and 72 hpi Vehicle-treated CPOs as the reference for Figure S4G.

QUANTIFICATION AND STATISTICAL ANALYSIS

All statistical tests and sample sizes are included in the Figure Legends and text. All data are shown as mean ± SEM or mean ± SD as stated in the Figure Legends. In all cases, the p values are represented as follows: ***$p < 0.001$, **$p < 0.01$, *$p < 0.05$, and ns, not statistically significant when $p > 0.05$. In all cases, the stated "n" value is either separate wells of monolayer cultures or individual organoids with multiple independent images used to obtain data points for each. No statistical methods were used to pre-determine sample sizes. For all quantifications of immunohistology, the samples being compared were processed in parallel and imaged using the same settings and laser power for confocal microscopy. For monolayer cultures, cells were segmented by first identifying nuclei, and then cytoplasmic area. Mean cytoplasmic intensities for SARS-CoV-2 nucleoprotein immunostaining were then measured in the segmented cytoplasmic regions, and a mean cytoplasmic intensity threshold was determined to identify SARS-CoV-2 infected cells. Cell numbers were then automatically counted for SARS-CoV-2 infected DAPI+ cells, and total DAPI+ cells. For brain organoids, immuno-positive cells were quantified manually using the cell counter function in ImageJ (NIH) or Imaris (Bitplane).